Electrocatalytic Oxidative Dehydrogenation of Propane in Solid Oxide Electrolysis Cells

Honors Undergraduate Thesis

Presented in Partial Fulfillment of the Requirements for the Honors
Research Distinction at The Ohio State University

By

Yingjie Shi

William G. Lowrie Department of Chemical and Biomolecular Engineering

The Ohio State University

2021

Thesis Committee:

Dr. Umit S. Ozkan, Advisor

Dr. Xiaoxue Wang

Abstract

Electrocatalytic oxidative dehydrogenation (ODH) of propane is a promising alternative method to steam cracking for propane production, due to its environmentally-friendly nature and lower operating temperature requirement. It also outperforms traditional catalytic dehydrogenation processes because the thermodynamic limitations are overcome, thereby enhancing propylene yields. In this study, the performance of dual phase composite perovskites consisting of electron and oxide ion-conducting strontium-doped lanthanum manganite (LSM) and proton-conducting ytterbium-doped strontium ceria (SCY) as the anode in a solid oxide electrolysis cell (SOEC) was investigated. The catalytic materials were characterized and analyzed via X-ray diffraction (XRD), X-ray photoelectron spectroscopy (XPS), diffuse reflectance infrared Fourier transform spectroscopy (DRIFT), X-ray absorption near edge fine structure (XANES), and temperature-programmed reaction/reduction (TPrxn/TPR). Propane ODH was carried out at 600°C in an SOEC with varied ratio of LSM and SCY in the anode. It was found that the selectivity towards proplyene was 24% for any anode composition. However, the alkene/CO_x selectivity increased with increasing SCY composition, indicating the presence of SCY could reduce the propane deep oxidation. It was observed that although pure LSM without the addition of SCY exhibited the highest conversion, it produced the most CO_x, possibly attributable to the reactive nature of LSM with propane. This study certified the feasibility of using electrocatalytic propane ODH to resolve the propylene supply and demand mismatch, but further investigations and development are needed to meet the standards of industrial-scale applications.

Acknowledgement

Vita

Oct. 22, 1998 . . . . Born, Shanghai, China

Autumn 2017 - Present . . . . Undergraduate Student

The Ohio State University, Columbus, Ohio

Publications

- D. J. Deka, J. Kim, S. Gunduz, D. Jain, Y. Shi, J. T. Miller, A. C. Co, U. S. Ozkan, Coke formation during high-temperature CO_2 electrolysis over $AFeO_3$ (A=La/Sr) cathode: Effect of A-site metal segregation, *Applied Catalysis: B 2020, 283, 119642*

- D. J. Deka, S. Gunduz, J. Kim, T. Fitzgerald, Y. Shi, A. C. Co, U. S. Ozkan, Hydrogen Production from Water in a Solid Oxide Electrolysis Cell: Effect of Ni Doping on Lanthanum Strontium Ferrite Perovskite Cathodes, *Industrial Engineering Chemistry Research 2019, 58(50), 22497-22505*

Contents

List of Figures

List of Tables

1 Introduction

1.1 Background

As the most produced olefins, ethylene and propylene contain some of the highest commercial values in the entire chemical industry [8]. These light olefins are extensively employed as building blocks for the production of polymers (polyethylene, polypropylene), oxygenates (ethylene glycol, acetaldehyde, acetone, and propylene oxide), and other derivatives (ethylbenzene, acrylonitrile, and propionaldehyde) [[10],[11]]. Many of these
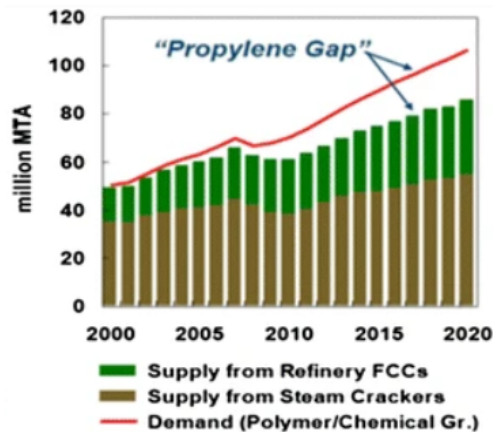
Figure 1: Propylene demand and supply gap [1]

compounds are crucial in the manufacture of major consumer goods, such as plastics, clothing, medical products, and aircraft materials [[8],[12]]. In recent decades, the global market of propylene has experienced an outpaced increase in demand relative to its supply, resulting in a growing mismatch between propylene supply and demand, namely a "propylene gap", as shown in Figure (1). The current leading technologies for propylene production are steam cracking and fluid catalytic cracking (FCC) of naphtha, light diesel, and other oil byproducts [[8],[10]]. Steam crackers account for 60-65% of the world's propylene production. Refinery FCCs account for other 30%, and the remainder is produced by on-purpose processes such as metathesis or propane dehydrogenation [1].

The hydrocarbon steam cracking process is carried out in tubular reactors suspended in a gas-fired furnace at elevated temperatures. This technology is considered well-established because of high optimization and increased capacities [13]. However, by using such method, the desired products have to be separated and purified from the effluent, which adds substantially to the capital costs. In addition, the inequivalence between the demand for

the product and the amount produced requires expenses on storage [14]. Along with these drawbacks, the declining crude oil reserves and increasing social awareness of the human impact have driven the exploration of alternative processes for propylene production with high efficiency and minimal environmental harm [13].

Propane is structurally similar to propylene except both C-H bonds are saturated. Propane dehydrogenation is a promising route to directly transform propane into propylene by stripping off hydrogen from propane molecules. Traditionally, propane can be obtained by natural gas processing and petroleum refining. Luckily, the significant advancements and refinements in fracking have promoted the efficient production of shale gas based natural gas liquids (NGLs) since 2008. While the shale gas provides abundant supply of light alkanes including propane, the development of such technology has caused their prices to drop sharply, thereby justifying the profitability of converting light alkanes into olefins through catalytic dehydrogenation. The on-purpose propylene production using the catalytic dehydrogentation method aims to yield propylene exclusively instead of a mixture of various light olefins, significantly reducing the costs spent on separation and purification in downstream. The reaction for propane catalytic dehydrogenation is described as follows:

$$C_3H_8 \longleftrightarrow C_3H_6 + H_2 \qquad \Delta H° = +109.31 kJ/mol \qquad (1)$$
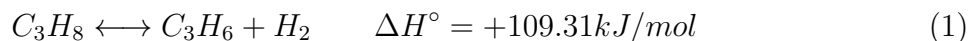
The predominant disadvantages associated with catalytic dehydrogenation include the thermodynamic equilibrium limitation and coke formation. As indicated by Equation (1), the high endothermicity under standard conditions necessitates intensive heat input to sustain the reaction. Negligible propane is converted at temperatures below 400°C, as shown in Figure (2). In order to achieve commercially feasible conversions, the reaction temperatures must exceed
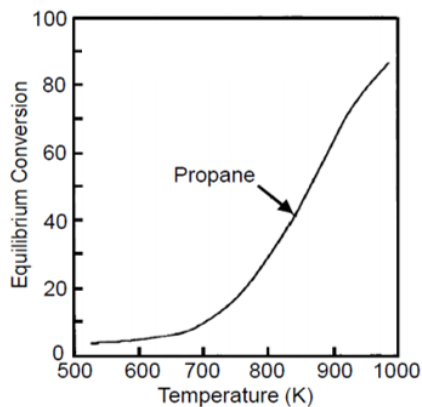

Figure 2: Thermodynamic equilibrium conversions of propane dehydrogenation vs. temperature [2]

2

600°C, which corresponds to a propane conversion of 40%. However, propane also starts to decompose at elevated temperatures, bringing about coke formation issues. Coking not only undermines propylene selectivity, but it also hinders heat transfer in the reactors, causing the inefficient use of energy [[15],[16]]. Furthermore, coking may even contribute to the decreased Faradaic efficiency in SOECs [17]. The coke formation is described as follows:

$$C_3H_8 \longleftrightarrow 3C + 4H_2 \qquad \Delta H° = +104.70 kJ/mol \qquad (2)$$
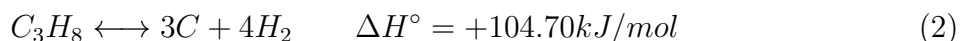
Oxidative dehydrogenation (ODH) is a potential solution to mitigate the thermodynamic limitation during catalytic dehydrogenation by co-feeding alkanes with gas-phase oxygen over packed-bed reactors. Oxygen serves to oxidize the H_2 evolved during dehydrogenation to water and is subsequently removed. The reduction in the concentration of any product could shift the equilibrium towards the product side based on Le Chatelier's principle. Hydrogen oxidation is a highly exothermic reaction, turning the overall oxidative dehydrogenation process from an endothermic into an exothermic one, which enables it to operate at lower temperatures. However, the oxygen-assisted pathway does not change the endothermicity of coking and cracking, meaning a lower operating temperature is effective to reduce the possibility of such side reactions. ODH yields little ethylene besides propylene, but ethylene is comparably valuable as propylene and is relatively easy to be separated. The primary reaction of an ODH process is illustrated as follows:

$$C_3H_8 + \frac{1}{2}O_2 \longleftrightarrow C_3H_6 + H_2O \qquad \Delta H° = -132.5 kJ/mol \qquad (3)$$

ODH improves energy efficiency compared to non-oxidative dehydrogenation because excessive heating and high pressure are not needed due to its thermodynamic favorability. Oxygen can also burn off the coke deposited on the catalyst, greatly improving heat transfer efficiency. Moreover, non-oxidative dehydrogenation processes require catalyst

3

regeneration for decoking purpose, but ODH is capable of a continuous operation without the such need [16]. Nevertheless, the selectivity control is a major concern for ODH, because molecular oxygen is a strong oxidant. High operating temperatures and high oxygen partial pressures inevitably lead to the over-oxidation of olefins to the form CO_2 and CO and limit olefin yields [8]. A certain ratio of oxygen and propane may even form an explosive mixture. The deep oxidation reactions are described by Equations (4),(5). In particular, the production of CO_2 can raise environmental concerns associated with greenhouse gas emission. Softer oxidants such as CO_2, N_2O, and SO_2 can be employed in place of oxygen. However, the biggest problems of using N_2O and SO_2 are safety hazards, like the risk of asphyxiation. The barrier of using CO_2 as an ideal softer oxidant arises from its low reactivity, thermodynamic stability, and high oxidation state [18]. Interestingly, the reaction mechanism of ethane oxidative dehydrogenation with N_2O involves the dissociation of N_2O molecules into predominantly O^- species on the catalyst surface, where O^- is the active form of oxygen for ethane dehydrogenation [19]. Hence, a reactor design that allows the reaction between hydrogen molecules and oxygen anions is promising to enhance selectivity while maintaining the thermodynamic advantages.

$$C_3H_8 + 5O_2 \longrightarrow 3CO_2 + 4H_2O \tag{4}$$

$$C_3H_8 + \frac{7}{2}O_2 \longrightarrow 3CO + 4H_2O \tag{5}$$
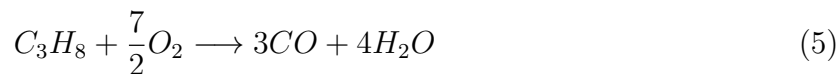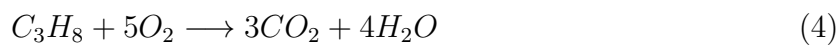
1.2 Solid Oxide Electrolysis Cells

1.2.1 Overview

A solid oxide electrolysis cell (SOEC) is an electrochemical reactor that supplies ionic oxygen to the catalytic reaction surface. The oxide ions are obtained from the dissociation of molecular oxidants, such as oxygen, over the cathode catalysts. The following equations suggest the mechanism of this process:

$$O_2(g) \longleftrightarrow O_2(ads) \tag{6}$$

$$O_2(ads) + 4e^- \longleftrightarrow 2O^{2-}(lattice) \tag{7}$$
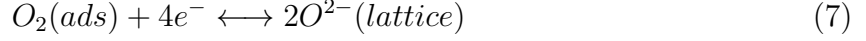
The setup of SOECs is similar to solid oxide fuel cells (SOFCs) in that both reactors are composed of a cathode, an anode, and an oxide ion-conducting electrolyte, but the major difference is that an external current is supplied to drive the reaction in SOECs, instead of producing electricity from chemical potential energy like galvanic cells such as

Figure 3: Three different modes of operation of a solid oxide electrolyte cell [3]

SOFCs. SOFCs usually require a high operating temperature above 600°C, but they are known to be highly efficient because their performance is not limited to Carnot efficiency due to the use of an external circuit [20]. Figure (3) shows the three operating modes of solid electrolyte cells. A positive current value means the current is being generated from the system and a negative value means the current has to be supplied for the operation. Our purpose in this study is to produce valuable substances instead of power. Hence, an electrolyzer mode (electrolysis cell) is utilized. The use of the electrolyte membrane can achieve a complete separation of reactant alkanes and molecular oxygen, preventing them from being mixed and avoiding deep oxidation. The electrolyte also serves as oxygen pumps and oxygen flux through the electrolyte is controlled by regulating the external current [8]. The relationship between oxygen flux and external current follows Faradaic coupling, as illustrated by Equation (8).
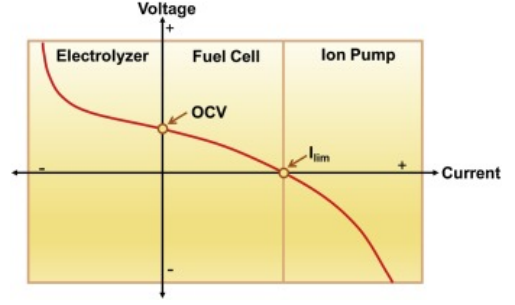
$$J = \frac{I}{nF} \tag{8}$$

where J is the oxygen flux in mol s^{-1}, I is the applied current in Amperes, n is the number of electrons transferred in the process in mol, and F is the Faraday's constant.

Earlier, our group conducted an experiment on electrocatalytically-assisted oxidative dehydrogenation of ethane in SOECs, which exhibited appreciable activity and accomplished as high as 14% ethane conversion and 10% ethylene yield with chlorine doped Ti-based perovskite oxide as the anode catalyst, proving this electrochemical process is viable. La doping on $SrTiO_3$ creates oxygen-rich planes in the crystal structure, and the chlorine radicals formed due to chlorine doping facilitates the decomposition of ethyl radicals to ethylene [8]. In this work, we intend to extend the research to propane ODH with the similar technology. However, each propane molecule contains two C-H bonds, adding difficulties for dehydrogenation because of its more complex molecular structure than ethane. Moreover, the presence of electrophobic π-bonds in propylene molecules is responsible for strong interactions with electron-deficient Lewis centers on catalytic oxide surfaces, resulting in highly adsorptive and reactive characteristics on the active sites of anode catalysts, which subsequently raises concerns about over-oxidation to CO_x [21]. Therefore, a different anode catalyst has to be explored.

SOECs feature the use of anionic oxygen rather than molecular oxygen as used in the packed-bed reactors in traditional ODH processes. This advancement minimizes the probability of alkene over-oxidation by supplying a softer oxidant. The design of propane ODH in SOECs aims to enhance propylene selectivity with low carbon footprint. The setup of SOECs can be visualized by Figure (4). The reaction scheme for electrocatalytic propane ODH on the electrodes is shown by Equations (9),(10).

Anode reaction:

$$C_3H_8 + O^{2-} \longrightarrow C_3H_6 + H_2O + 2e^- \tag{9}$$

Cathode reaction:

$$\frac{1}{2}O_2 + 2e^- \longrightarrow O^{2-} \tag{10}$$
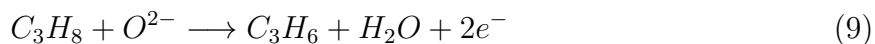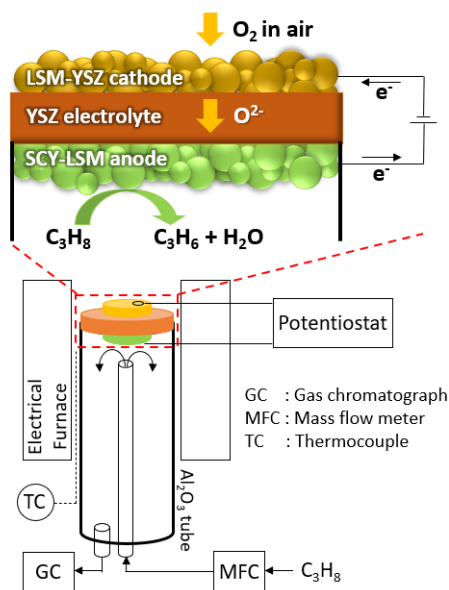
Figure 4: The setup of an SOEC for propane ODH

1.2.2 Electrolyte

An ideal electrolyte for SOECs should exhibit excellent ionic conductivity at elevated temperatures. Meanwhile, it is required to reject electron transfer to prevent short circuit, so minimal electrical conductivity is desired. Figure (5) compares the oxide ion conductivity for various commonly used electrolytes in SOFCs and SOECs as a function of temperature. Pure zirconium dioxide transforms from a monoclinic crystal structure to tetragonal at 1170°C. A desired stable structure is cubic, but the phase shift of tetragonal-cubic requires 2370°C. However, doping ZrO_2 with soluable aliovalent oxides such as CaO, MgO, or Y_2O_3 allows it to exhibit cubic phases even at room temperature [22]. Among these, yttria-stabilized zirconia (YSZ) is widely used in the constitution of both SOECs and SOFCs at high temperatures (800 - 1000°C). YSZ demonstrates remarkable thermal stability, corrosion resistance, mechanical strength, and durability [[22],[23]]. Most importantly, its oxide ion conductivity is enhanced at high temperatures because of the replacement of Zr^{4+} with Y^{3+} creates vacancies inside the lattice, thereby allowing the oxide ions hopping through the lattice, which results in high concentration of oxide ions and high mobility

7

of oxygen vacancies [24]. The highest oxide ion conductivity can be achieved when the composition of Y_2O_3 reaches 8%. In other words, $Zr_{0.92}Y_{0.08}O_{2-\delta}$ exhibits the optimal oxide ion conductivity among YSZ derivatives. However, the ionic conductivity of YSZ drops significantly with decreased temperatures. At intermediate or low temperature SOFCs, YSZ must be fabricated in a thin-film form to compensate the lowered ionic conductivity [23]. The biggest drawback of using YSZ is the incompatibility with perovskite electrodes that contain cobalt, due to their thermo-mechanical mismatch [25]. An alternative electrolyte to YSZ at moderate temperatures (600-700°C) is gadolinium-doped ceria (GDC). Similar to YSZ, oxygen vacancies in CeO_2 can be introduced by doping rare earth oxides, such as Y_2O_3, Gd_2O_3, Sm_2O_3, and Nd_2O_3. The outstanding oxide ion conductivity of GDC is attributed to presence of oxygen vacancies due to the substitution of trivalent ions (Ce^{3+}) by tetravalent ions (Gd^{4+}). GDC is considered to be one of the best ceria-based solid electrolytes and is widely used in the temperature range where YSZ shows degraded conductivity or the electrode materials are intolerant with YSZ [26]. In this work, even though the operating temperatures are not in the optimal range for YSZ, our study utilizes YSZ as the electrolytes in the thin-film form.

1.2.3   Perovskite oxides as electrode catalysts

Perovskite oxides are a class of materials in the mixed-oxide family. They have received substantial research interests because of their exceptional thermal stability, electonic structure, ionic conductivity, electron mobility, and redox behavior. Perovskite oxides have a general formula of ABO_3, where A and B commonly denote large-sized 12-coordinated
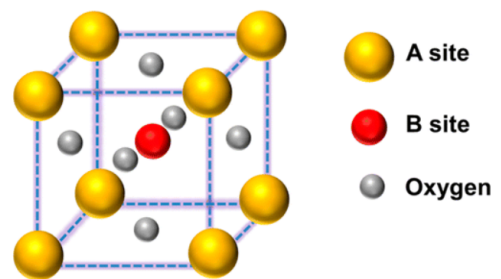
Figure 6:   Schematic illustration of an ideal ABO_3 perovskite unit cell [4]

cations and small-sized 6-coordinated cations, respectively. In general, the properties of perovskite oxides are determined by the nature of the B-site cations, because they play

8
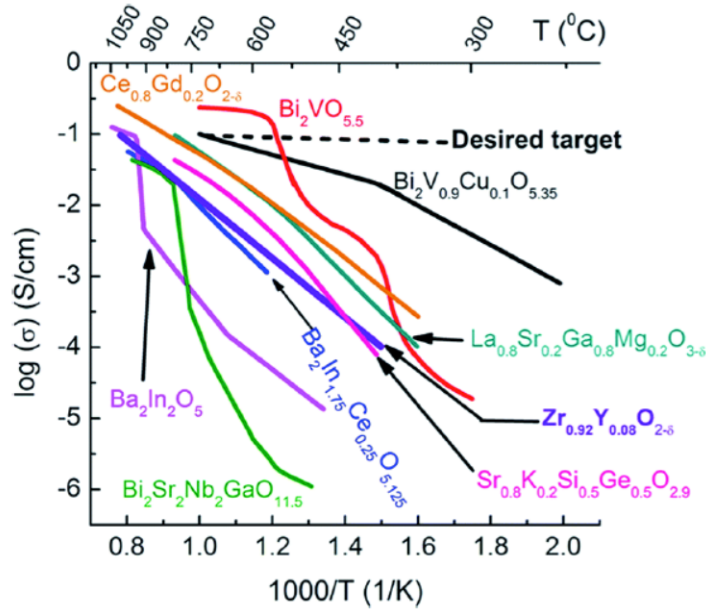
Figure 5: Oxide ion conductivity of variouos electrolytes as a function of temperature [5]

essential roles in altering the electronic structure of the perovskite oxides, thus affecting the catalytic process [4]. Sites A and B are versatile to accommodate different metal ions over a wide range, as shown in Figure (7). However, for stability considerations, the relative ionic sizes of A and B sites in the perovskite system are constrained. The ionic radii of A and B cations need to follow the resistance criterion of Goldschmidt described by Equation (11), where t represents the tolerance factor. A t-factor value in the range of 0.75 to 1 guarantees the crystallinity of the perovskite oxides. The structures of perovskites vary in cubic, orthorhombic, rhombohedral, tetragonal, monoclinic, and triclinic symmetries, depending on the value of the t-factor [6].

$$t = \frac{(r_a + r_O)}{\sqrt{2} \times (r_B + r_O)} \tag{11}$$

Because of the minor effects of the A site cations on catalysis, lanthanum-based perovskite oxides have been the most frequently studied [4]. A complete perovskite structure can undergo modifications by rational doping on the A and/or B sites. By doing so, the oxygen content in the structure is reduced, thus introducing oxygen vacancies and oxygen-

9
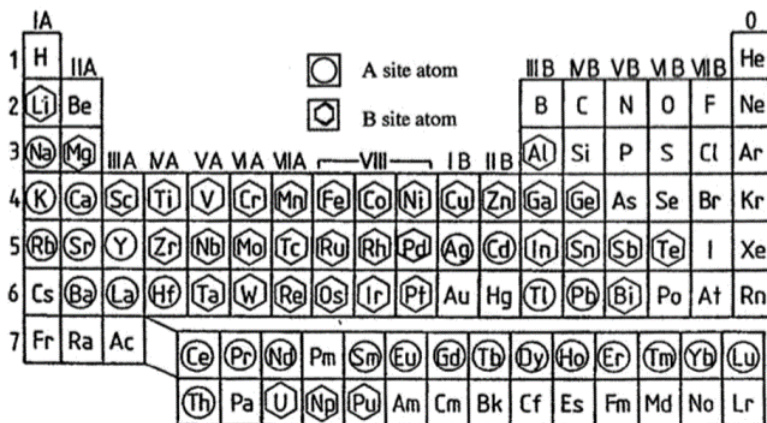
Figure 7: Chemical elements that can occupy sites in the perovskite structure [6]

rich pales, which subsequently enhances its ionic conductivity, electronic conductivity, and/or catalytic activity [27]. The most commonly dopant on the A site of lanthanum-based perovskite oxides is Sr owing to its matched atmoic size with La. The difference in the charges of these two atoms leads to oxygen nonstoichiometry in the perovskite structure, resulting in improved oxygen mobility [4].

1.2.4 Cathode

A good candidate for electrodes used in SOECs requires decent electrical conductivity to reduce ohmic resistance across the electrodes, ensuring the efficient use of electrical power. High oxide ion conductivity has to be incorporated as well to allow effective oxide ion transfer. Metallic oxides preserve both electrical and oxide ion conductivity and are highly durable at elevated temperatures, rendering them ideal materials for the electrodes. Strontium-doped lanthanum manganite (LSM) perovskite oxide is extensively used as the appropriate electrode materials in large-scale SOFCs in the range of 700-900°C. This is because its excellent electrical conductivity, strong electrochemical activity for the reaction of O_2 reduction, and reliability over a long operational period [28]. In this work, A-site deficient $(La_{0.8}Sr_{0.2})_{0.95}Mn_{3-\delta}$ is mixed with YSZ at equal weight. The A-site cation deficiency increases its oxide ion conductivity in addition to its remarkable electrical conductivity. The addition of YSZ to the LSM-YSZ composite electrode significantly enhances the catalytic

10

activity. Moreover, the mixture grants enhanced thermal compatibility between the cathode and the YSZ electrolyte by means of the improved adhesion due to the intimate sintering of YSZ particles to LSM-YSZ substrate [23].

1.2.5 Anode

Since the partial oxidation of propane takes place over the anode catalyst, the ODH performance is heavily dependent on the catalytic activity of the anode material, thus it is the research target in this study. Proton-conducting perovskite materials have received substantial research interests due to their great advantages, such as low activation energy and high energy efficiency [29]. Hydrogen molecules dissociate into protons and emit electrons onto the active anode layers. The protons subsequently interact with the oxygen ions transferred from the cathode to form water molecules. Perovskites from the family of ABO_3 (A=Ba, Sr / B=Zr, Ce) represent the most attractive proton-conducting catalytic materials. $BaCeO_3$-based proton conductors exhibit the highest protonic conductivity in addition to increased oxide ion conductivity at with increasing temperature. $SrCeO_3$-based proton conductors tend to exhibit dominating protonic conductivity in hydrogen or steam atmosphere mainly because of the suppression of oxygen ionic conduction within its distorted orthorhombic structure. In applications of hydrogen transport, $SrCeO_3$ tends to outperform $BaCeO_3$ to be a more suitable material [30]. Both Ba and Sr-based cerates have orthorhombic perovskite structures and become close to cubic symmetries at high temperature. Their protonic conductivity is associated with the degree of variation in their crystallographic symmetry from an ideal cubic structure [31]. Oxides of Yb and Y are typically doped into the $SrCeO_3$ structure to further enhance protonic conductivity at high temperatures. It has been reported that $SrCe_{0.95}Yb_{0.05}O_{2.975}$ (SCY) in hydrogen at approximately 950°C has a conductivity of $10^{-2}\Omega^{-1}cm^{-1}$, which is superior to any other proton conductors [32]. The performance of propane ODH is intimately correlated to the efficient removal of hydrogen. Remarkable protonic conductivity is necessary to guarantee

such efficiency. Therefore, the use of SCY in the anode composite is rationalized.

Once a hydrogen molecule is captured by an adjacent lattice oxygen, an OH$^-$ ion is formed and the proton attached to the O^{2-} can migrate between the oxide ions, thereby contributing to the protonic conductivity of the perovskite. A possible proton conduction mechanism is illustrated in Figure (8). The proton starts with attaching to O1 at position 1. It gets attracted to O2 and the bond between the Ce cation and O1 bends. The shortened bond length between O1 and O2 reduces the energetic barrier for
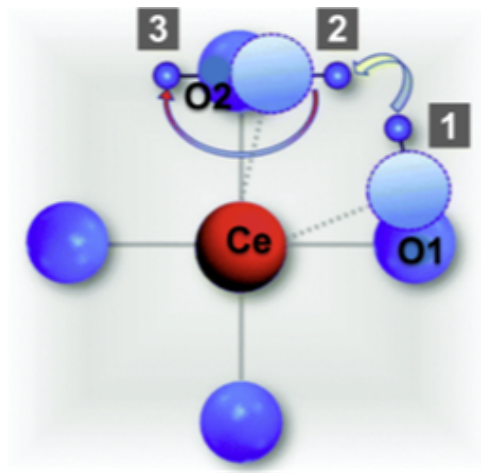
Figure 8: A possible mechanism for proton conduction in SCY [7]

proton transfer, allowing the proton to hop from O1 to O2 and to form a bond with O2. In this position, the proton can move towards another oxide ion likely by means of rotation motion around the bond between O2 and Ce-O$_2$. By repeating the same process of bending, hopping, and rotational motions, the proton can be transferred to other oxide ions [7].

Besides the existence of proton conduction mechanism, elements Ba and Sr are strongly basic. Therefore, Ba and Sr-based cerates are known to have abundant basic sites. Although high basicity is required to facilitate prompt desortpion of the adsorbed alkenes due to the presence of electrophobic π bonds, it can also lead to a reaction between the catalytic active sites and acidic molecules such as CO_2, which can be formed as a consequence of over-oxidation during propane ODH. The interaction of Ba and Sr sites with CO_2 might form $BaCO_3$ and $SrCO_3$ second phases. The deposition of these catalytic inactive species will undermine the activity of the catalytic sites. To mitigate this, the basicity of these cerates can be tuned by replacing some of the B site ions by more electronegative ions, thereby achieving the optimization between product selectivity and material stability.

As discussed previously, an ideal electrode catalyst requires sufficient electrical con-

12

ductivity to enhance the efficiency of cell operations. It has been reported that ytterbium-doped strontium cerate ($SrCe_{1-x}Yb_xO_3$) is an appreciable catalyst for ethane ODH at 500-700°C [33]. Hence, the incorporation of proton-conducting phase into oxide ion-conducting anode catalysts is a reasonable approach to achieve high propane ODH performance. As introduced earlier, one of the main challenges of propane ODH lies in the deep oxidation of hydrocarbons to carbon oxides. Therefore, excessive oxide ion-conductivity may contribute to the production of undesired products, thereby rationalizing the use of moderate oxide ion-conductive but high electrical-conductive perovskites, such as $La_{1-x}Sr_xMnO_3$ and $La_{1-x}Sr_xTiO_3$. In the light of these views, this study intends to develop a dual phase perovskite oxide composite consisting of ytterbium-doped strontium cerate (SCY) and strontium-doped lanthanum manganite (LSM) for propane electrocatalytic ODH.

2 Experimental

2.1 Synthesis

Perovskite-type materials ytterbium-doped strontium cerate ($SrCe_{0.95}Yb_{0.05}O_{3-\delta}$) and strontium-doped lanthanum mangnite (($La_{0.8}Sr_{0.2})_{0.95}MnO_{3-\delta}$) were synthesized via an Ethylenediaminetetraacetic acid (EDTA) - citric acid complexation route, as demonstrated in Figure (9). Stoichiometric amount of strontium carbonate ($SrCO_3$), cerium nitrate hexahydrate ($Ce(NO_3)_3 \cdot 6H_2O$), and ytterbium nitrate pentahydrate ($Yb(NO_3)_3 \cdot 5H_2O$) were first dissolved in deionized water. The chelating agent, EDTA, was added to the solution in a stoichiometric ratio of 1.5:1 with respect to metal ions. The solution was heated to 40 °C on a heating plate with a water bath

Figure 9: Flowsheet of EDTA-citric acid complexation route for SCY synthesis

under uniform stirring. Meanwhile, ammonium hydroxide (NH_4OH) was added drop-wise to adjust the pH. Once EDTA powders were fully dissolved, citric acid was added to the solution in a stoichiometric ratio of 1:1 with respect to metal ions. The temperature of the solution was gradually increased to 80 °C, while continuing adding NH_4OH to maintain the pH at approximately 6 in order to hinder hydrolysis reaction. The solvent evaporation was accompanied by the formation of transparent gel, which was dried at 200 °C overnight and then calcined at 1000 °for 3 h and 15 min with a 5 °C min^{-1} ramp rate. The calcination scheme is illustrated by Figure (10). LSM was synthesized through the same procedure

but the precursors used were lanthanum nitrate hexahydrate ($La(NO_3)_3 \cdot 6H_2O$), strontium nitrate ($Sr(NO_3)_2$), manganese nitrate tetrahydrate ($Mn(NO_3)_2 \cdot 4H_2O$). In addition, the calcination temperature used was 700 °C.
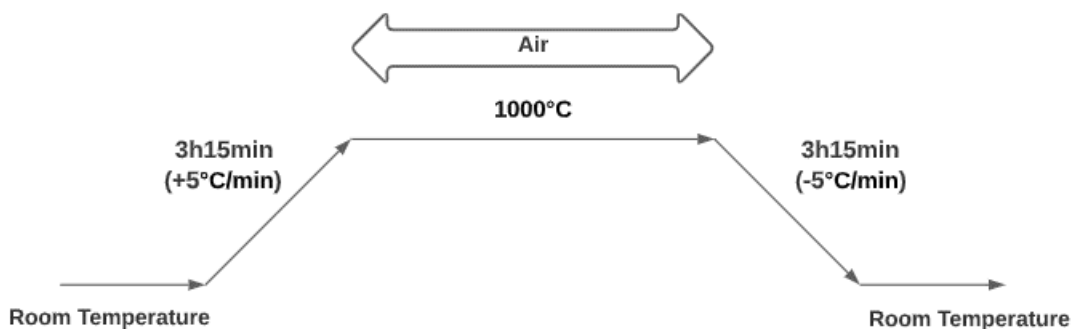
Figure 10: SCY calcination scheme

2.2   Button Cell Fabrication

The button cell refers to the assembly of electrode-electrolyte, namely the solid oxide electrolysis cell. First, a circular disc of 1-inch outer diameter was punched out of a YSZ tape-casted sheet obtained from ESL Electroscience Laboratory. After densification in air at 1450°C in air, the thickness of the YSZ disc reached 125 μm. A slurry mixture of LSM and SCY powders with various weight ratio (2:8, 4:6, 6:4, 8:2) was prepared by using an ink vehicle (NexTech Materials) and was then screen printed onto one side of the densified electrolyte. Sintering was performed for the anode deposited layer at 1200°C. Next, a slurry of LSM-YSZ (NexTech Materials) cathode with 1:1 weight ratio was screen printed on the other side of the YSZ disc. The disc was fired at 1200°C, which resulted in an electrode thickness of ~25 μm.

Gold wires (0.1 mm O.D., 99.99% trace metal basis, Sigma Aldrich) were attached onto both electrodes using 8880-G high temperature conductive gold paste (ELS Electroscience) and dried at 100°C in air for 1 h. The gold leads served as current collectors. These cells were sealed on top of an alumina (2.54 cm O.D.) tube by pasting Schott GM 31107^{TM} glass

seal, with the anode facing inside the tube. The glass seal was dried at 125°C and heated to 350 °C at 3°/min and held for 90°min to remove binders, then heated to 700°C at 2°C/min and cured for 30 min. After curing, the silver wires were connected to a potentiostat, which was composed of a Keithley 6220 current source for current application and a Keithley 6182 voltmeter for voltage measurement via silver leads (0.64 mm O.D., 99.9% metals basis, Alfa Aesar). The setup can be visualized in Figure (11). When conducting the electrocatalytic ODH experiments, 2 sccm of 5% propane/He was fed to the anode, and these conditions were maintained for 12 h to ensure the stability of operation parameters, including pressure, temperature and reactant flow. The outlet of the reactor was separated and analyzed by the Shimadzu GC 2014.
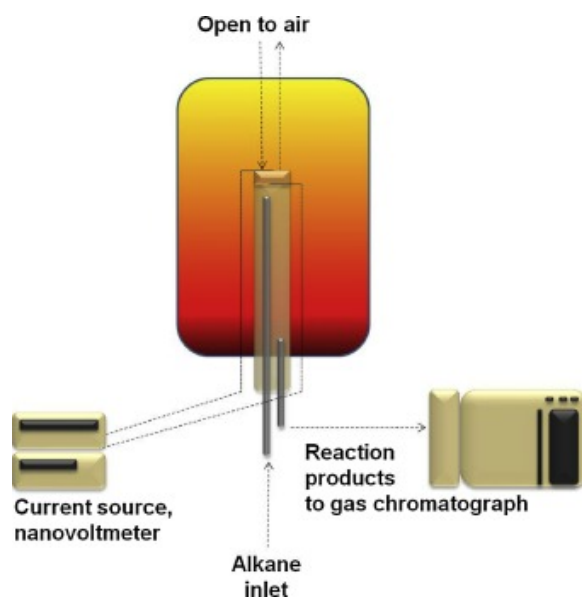
Figure 11: Electrochemical propane ODH button cell setup [8]

2.3 Characterization

2.3.1 X-Ray Diffraction (XRD)

The powder X-ray diffraction patterns for the synthesized samples were collected using a Bruker D8 Advance X-ray powder diffractometer operated at 40 kV and 40 mA with a step size of 0.014°per 0.75 s in the 2θ range between 20°and 60°. A typical XRD pattern for $SrCeO_3$ can be indexed as an orthorhombic structure with space group $Pbnm$, $Z=4$ at room temperature. The partial substitution of Ce by trivalent cations, such as Yb, would introduce the simultaneous occurrence of p-type electrical and oxide ion conductivity and appreciable protonic conductivity [34]. A structural phase change or precipitation of an impurity phase due to the existence of Yb could be revealed by XRD. Generally, the lattice parameters can be obtained by Bragg's law, as described below:

$$n\lambda = 2d\sin\theta \tag{12}$$

where n is the order of reflection, λ is the wavelength of the incident wave, and d is the spacing between the parallel planes or atoms. In our study, the unit cell dimensions of the catalyst powders were determined by the least square refinement from the UnitCell software [35]. The average crystallite sizes of the catalysts were estimated using the Scherrer equation shown below as Equation 13.

$$D = \frac{K\lambda}{B\cos\theta} \tag{13}$$

Here, K is the shape factor, with a typical value of about 0.9, λ is the wavelength of Cu-Kα (1.54059 $\mathring{A}$), θ is the angle of Bragg diffraction and B is the full width at half maximum (FWHM) of the most intense peak.

2.3.2 X-Ray Photoelectron Spectroscopy (XPS)

XPS is a surface sensitive technique based on photoemission effect. A monochromated Al Kα source (12kV, 10mA) or a Mg Kα source (1254 eV, 12kV, 10 mA) and a charge neutralizer at 2.1 A, 1.3 V bias were obtained from a Kratos Ultra Axis Spectrometer, which would incident on the surface of the catalysts. A charge of 2.6 V was used and a survey scan was collected from 1200 eV to 0 eV. The photoelectrons emitted from the samples would provide specific information on the elemental composition and electronic and chemical states on the near surface ($\sim$10 nm) of the catalysts. Since the surface represents a discontinuity between one phase and another and the elemental composition and electronic and oxidation states at the surface were differed from those of the bulk phase, many surface phenomena, such as catalysis and adsorption/desorption behaviors, should be investigated by XPS, which provides information on the oxidation state changes of Sr, Ce, and Yb on the surface of SCY catalysts [36].

2.3.3 X-ray Absorption Spectroscopy (XAS)

XAS reveals the specific bulk structure of the samples. This technique provides two divided absorption spectra: X-ray Absorption Near Edge Fine Structure (XANES), which elucidates the oxidation states of the elements in the catalysts, and Extended X-ray Absorption Fine Structure (EXAF), which informs the coordination number and bond length of the targeted element with neighboring atoms. In this study, XANES data were collected at sector 10-BM of the Materials Research Collaborative Access Team (MRCAT) at the Advanced Photon Source (APS, Argonne National Laboratory). *Ex-situ* measurements on the catalyst powders were done in transmission mode. The samples were mixed with BN in the weight ratio of 1:5, ground well, and pressed into a sample holder containing cylindrical hole of 0.12 cm^2 cross sectional area. Each measurement on the sample was coupled with X-ray absorption spectra of the corresponding metal foil to calibrate the data for any shift

in X-ray energy.

2.3.4 Diffuse Reflectance Infrared Fourier Transform Spectroscopy (DRIFTS)

DRIFTS is a surface sensitive technique used to obtain the rotational and vibrational bond energies associated with molecular species adsorbed on the surface of a solid sample. DRIFTS studies were performed using a Thermoelectron Nicolet 6700 FTIR equipped with a MCT detector and a Praying Mantis chamber capable of measurements under controlled environment and temperature. Spectra were collected in the mid-infrared region of 4000-7000 cm^{-1}, where molecular vibrations can be observed. The methanol adsorption was performed by introducing methanol via bubbling 30 sccm He through pure methanol and sending to the sample for 1 h at 50°C. Methanol probe molecules were bounded to Lewis acid site and dissociatively adsorbed on basic sites. Next, a similar procedure was done for pyridine adsorption experiments. Pyridine probe molecules were used to identify the presence of Lewis as well as Bronsted acidic sites from coordinated pyridine, hydrogen-bonded pyridine, and the pyridinium ion, respectively.

2.3.5 Temperature-Programmed Reaction/Reduction (TPrxn/TPR)

TPrxn experiments were conducted to investigate the interaction characteristics between catalysts and reactants as a function of temperature. 30 sccm 5% propane/He was sent to SCY and LSM sample powders, respectively, with a programmed heating rate of 10°C/min to 700°C and held for 1 h. The degree of reducibility of each catalyst as a function of temperature was also studied by TPR experiments, which were carried out at a 30 sccm 5% H_2/N_2 flow and a programming heating rate of 10°C/min to 1000°C and held for 1 h. The gas outlet from the reactor was fed to an MKS Cirrus bench-top residual gas analyzer, with mass signals of 1-100 monitored throughout the experiment.

2.4 Electrical Conductivity and Activation Energy

In this study, high electrical conductivity of the catalytic electrodes is desired in order to prevent the excessive use of energy and unnecessary ohms. The electrical conductivity of the catalyst samples was measured by applying the 4-probe DC van der Pauw technique. The post-calcined powders were pelletized into rectangular bars using a hydraulic press and sintered at 1300 °C for 12 h to obtain dense pellets. Four silver wires (0.1 mm) were attached to
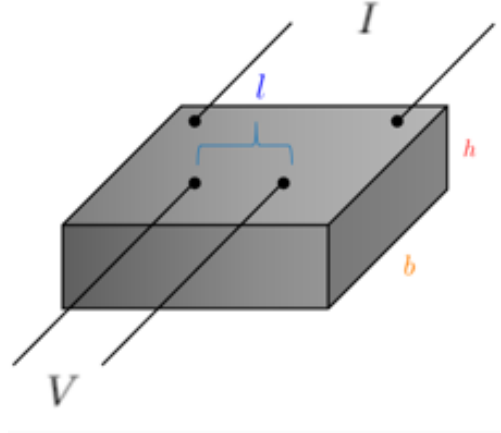
Figure 12: The electrical configuration for the 4-probe DC van der Pauw method [9]

the pellets using Pelco™ High Performance silver adhesive paste. A keithley 6220 current source was used to apply current to the outer silver leads. The corresponding voltage was measured by a Keithley 6182 sensitive nanovoltmeter from the inner leads. The electrical configuration for the electrical conductivity measurement technique is shown in Figure (12). Measurements were taken in the range of 100 to 600°C for various SCY-LSM compositions. The electrical conductivity, σ, was calculated by Equation 14 shown below:

$$\sigma = (\frac{I}{V})(\frac{l}{A}) \tag{14}$$

where I is the applied current, V is the potential difference between the measured and the background, l is the distance between the voltage leads, and A is the cross-sectional area for the current flow and is the product of b and h shown in Figure (12). The conductivity values were then averaged over multiple readings at each temperature.

Conductivities of SCY and LSM were expected to increase with an increasing temperature, and reach a maximum at a certain temperature and drop at higher temperatures. For LSM, the drop can be explained by the oxygen vacancy formation process that takes place due to heating LSM perovskite oxide [37]. This can be denoted by the Kröger-Vink

notation as shown in Equation (15).

$$(La_{0.8}^{\times}Sr_{0.2}^{'})_{0.95}Mn_{0.66}^{\times}Mn_{0.34}^{\bullet}O_{3}^{\times} \Longleftrightarrow (La_{0.8}^{\times}Sr_{0.2}^{'})_{0.95}Mn_{0.66+2\delta}^{\times}Mn_{0.34-2\delta}^{\bullet}O_{3-\delta}^{\times}[\delta V_{O}^{\bullet\bullet}] + \frac{\delta}{2}O_{2}$$

$$(15)$$
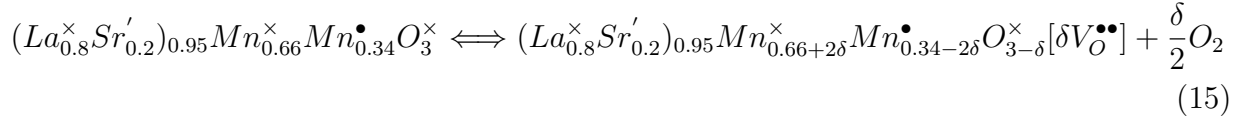
In the equation above, '$\times$' denotes neutral effective charge, "'" denotes a negative effective charge, '$\bullet$' denotes a positive effective charge, and '$V_{O}^{\bullet\bullet}$' is an an oxygen vacancy having two effective positive charges. Doped lanthanum strontium manganite possibly exhibits p-type conduction following a small polaron conduction mechanism, just like lanthanum strontium ferrites [38], but doped strontium cerate demonstrates no such conduction mechanism. From the calculated electrical conductivity for each sample under various temperature, the activation energy for the hopping of polarons for each sample was determined according to Arrhenius-type Equation (16).

$$\sigma = \frac{A}{T}exp(-\frac{E_a}{kT})$$

$$(16)$$

Here, A is a pre-exponential factor that depends on material property and charge carrier density, E_a is activation energy for the hopping of polarons, k is the Boltzman constant, and T is the absolute temperature in Kelvin. By plotting the natural logarithm of σT against $1/T$ and performing a linear fit, the slope of the straight line is numerically equal to E_a/k. The activation energy in eV could be solved thereafter. Equation (17) shows the numerical relationship between E_a (in eV) and the slope of the linear fit.

$$E_a = -slope \times 8.6173303 \times 1000 \times 10^{-5}(ev)$$

$$(17)$$

3 Results and Discussion

3.1 XRD

Figure (13) shows *ex-situ* powder XRD patterns of the thermochemically treated samples before and after reduction treatment with 5% H_2/N_2 at 800 °C for 1 h. The pre-treated strontium-doped lanthanum manganite (LSM) has a rhombohedral perovskite structure in the space group R$\bar{3}$c with no impurity phases. The XRD pattern of the synthesized LSM sample with slight A-site deficiency is consistent with that of the A-site stoichiometric LSM prepared from sol-gel suggested by literature [39]. Ytterbium-doped strontium ceria XRD pattern shows a distorted orthorhombic perovskite crystal structure with a space group *Pbnm* at room temperature, and is likely to transform into cubic symmetry at above 800°C [40]. The result matches the XRD pattern reported by literature [41]. Both samples remain intact in the reducing environment, with no introduction of impurity phases, indicating their excellent thermochemical stability. The peaks of reduced SCY sample are slightly shifted towards lower 2θ values, possibly attributable to unit cell expansion. The lattice parameters and crystallite sizes of SCY and LSM are summarized in Table (1). Interestingly, the lattice parameters for SCY are similar to the reported values for undoped $SrCeO_3$, but doping Yb is expected to change the symmetry and result in a larger b value [41]. Presumably, doping Yb in our synthesized SCY sample does not alter the structure for some reason. The lattice parameters a and b for LSM are similar to the reported values, but the calculated value of c in this study is much smaller than 13.3678 $\mathring{A}$ [39]. The disparity is probably due to the effect of A-site deficiency in our sample.

Catalyst	Crystallite size (nm)	a($\mathring{A}$)	b($\mathring{A}$)	c($\mathring{A}$)
$SrCe_{0.95}Yb_{0.05}O_{3\,-\delta}$	24.10	6.080	5.966	8.561
$(La_{0.8}Sr_{0.2})_{0.95}MnO_{3-\delta}$	23.81	5.689	5.693	7.086

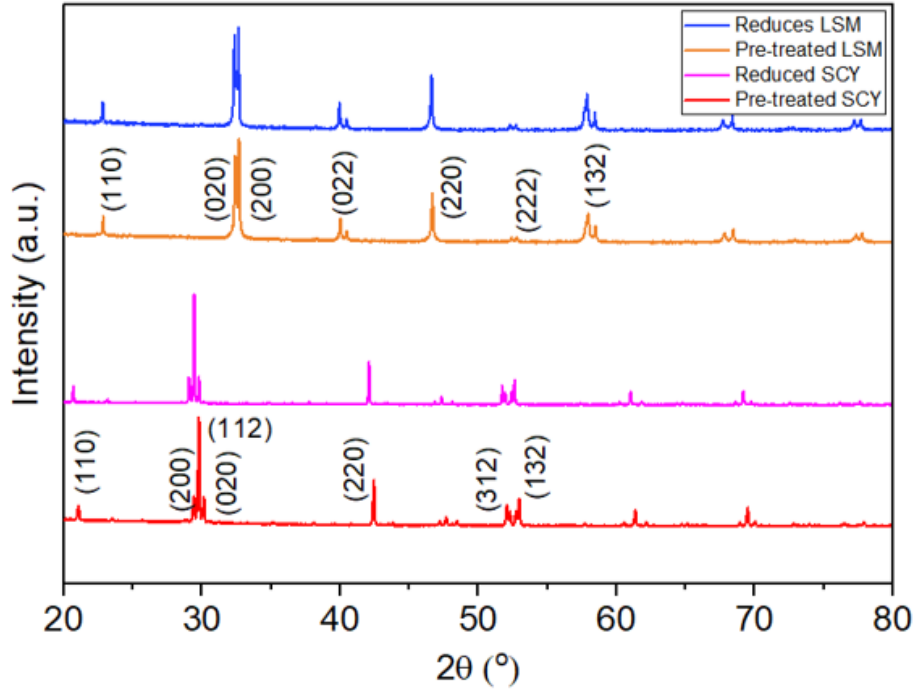**Table 1:** Crystallite sizes and lattice parameters of SCY and LSM

Figure 13: XRD pattern of pre-treated and reduced samples

3.2   XPS

XPS measurements were conducted to investigate the oxidation states of metal ions and the atomic concentrations on sample surfaces. The electronic angular momentum number can be expressed by $j = I + s$, where I is the angular momentum quantum number, and s is the spin angular momentum number and can be $\pm\frac{1}{2}$. Therefore, for the $2p$ spectra of Ce, there exists two spin orbit peaks, namely $2p_{1/2}$ and $2p_{3/2}$. Similarly, the spin orbit peaks for Mn $3d$ spectra are $3d_{3/2}$ and $3d_{5/2}$. The peaks have specific area ratios based on the degeneracy of each spin state, with 1:2 for $2p_{1/2}$: $2p_{3/2}$ and 2:3 for $3d_{3/2}$: $3d_{5/2}$ [42]. The concentration of surface metal ions was calculated based on the area ratio for each spin orbit peak. The results are summarized in Table (2). The Ce^{4+} concentration in the pre-treated SCY is observed to be 89.3%. After reduction treatment with 30 sccm 5% H_2/N_2 for 1 h at 600 °C, XPS spectra show a slight drop in the Ce^{4+} concentration to 86.9%. An increase in the temperature to 850°C under the same reducing environment

23

further reduces the Ce^{4+} concentration to 76.4% because of the presence of more abundant Ce^{3+}. The increase in the Ce^{3+} with respect to temperature can be graphically seen by the increase in the area under the peaks at 901.5eV, 895.4eV, 883.4eV, and 879.2eV, as shown in Figure (14). Over the heating process, the average oxidation state of Ce decreases from 3.89 for pre-treated samples to 3.76 for reduced samples at 850°C.
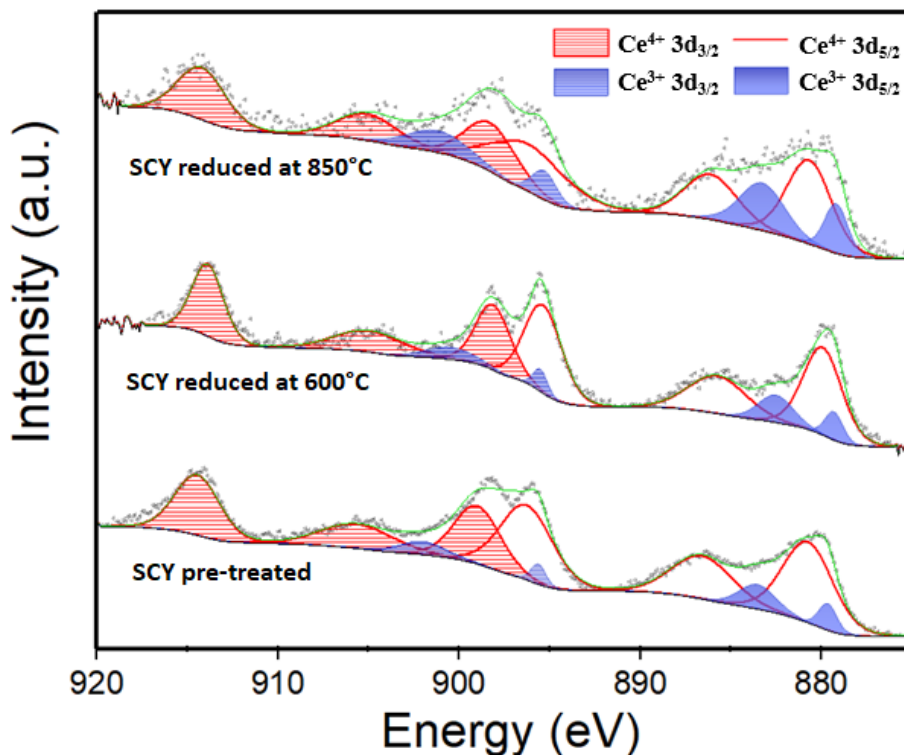
Figure 14: XPS spectra of SCY

In comparison, the concentration of Mn^{4+} experiences a sharp drop, from 62.8% for pre-treated to 19.5% for reduced at 850°C. The average oxidation state of Mn decreases significantly, from 3.63 to 3.20. It can be seen that there is a much larger increase in the area below the peaks at around 651.5eV and 640eV, as shown in Figure (15). An average oxidation state drop of 0.43 for Mn in LSM relative to a drop of 0.13 for Ce in SCY indicates that LSM has much stronger reducibility and thus qualifies a better oxide ion and electron conductor. In addition, an average oxidation state as low as 3.20 of Mn reflects the reactive nature of reduced LSM at 850°C.
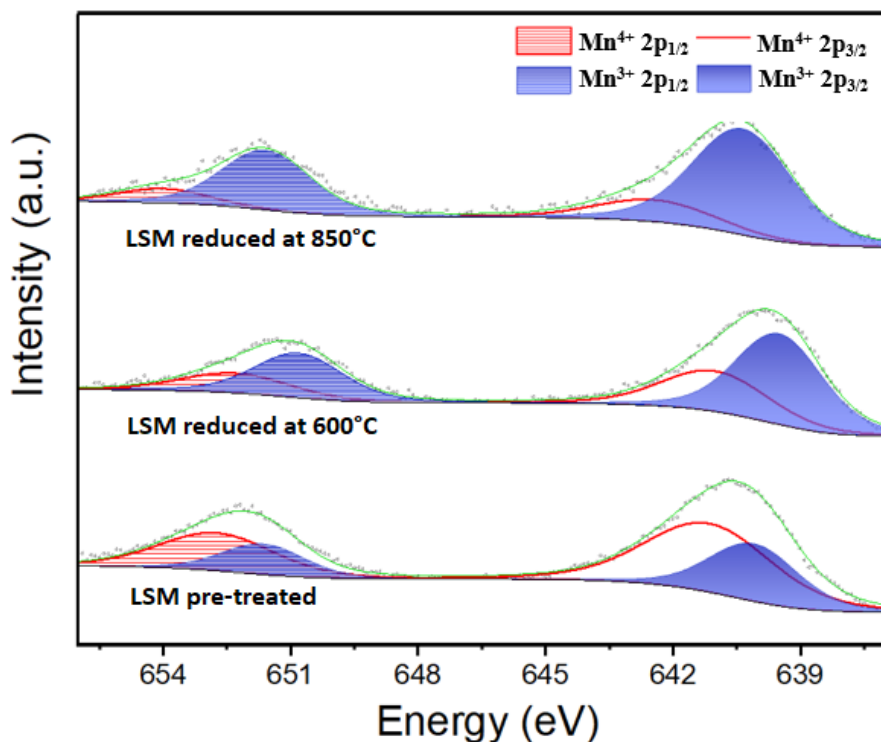
Figure 15: XPS spectra of LSM

	Ce^{3+}		Ce^{4+}		
	Concentration (%)	3d 5/2 Position (eV)	Concentration (%)	3d 5/2 Position (eV)	Avg. oxidation state
SCY reduced at 850°C	23.6	879.2	76.4	880.7	3.76
SCY reduced at 600°C	13.1	879.4	86.9	880.0	3.87
As-calcined SCY	10.7	879.7	89.3	880.7	3.89
	Mn^{3+}		Mn^{4+}		
	Concentration (%)	2p 3/2 Position (eV)	Concentration (%)	2p 3/2 Position (eV)	Avg. oxidation state
LSM reduced at 850°C	80.5	640.0	19.5	642.1	3.20
LSM reduced at 600°C	64.9	639.1	35.1	640.6	3.35
As-calcined LSM	37.2	640.1	62.8	641.1	3.63

Table 2: A summary of XPS results

3.3 XANES

XANES spectra were obtained to investigate the average oxidation states and chemical identities on the basis of the electronic structure of the probing atoms. Figure (16) shows the normalized Ce L$_3$-edge XANES spectra of SCY with standard Ce compounds. The dipole $1s \rightarrow 3d$ transition permitted after combining the metal d with $4p$ states gives rise to the characteristic pre-edge peak. The strong single absorption peak (5722 eV) of Ce^{3+} ions on the reference Ce(NO$_3$)$_3$ is caused by the $2p_{3/2} \rightarrow 5d$ transition according to the dipole selection rules. The absorption spectra of Ce^{4+} ions on the reference CeO$_2$ consists of two distinct peaks. The lower energy peak (5733eV) is attributed to the $2p_{3/2} \rightarrow (4f - L)5d$, and the higher energy peak (5740eV) is caused by the $2p_{3/2} \rightarrow 5d$ transition [43]. The edge energies of Ce ions in SCY powders are found as between Ce^{3+} (5719.6eV) and Ce^{4+} (5728.0eV). The edge energy of Ce ion from the reduced SCY at 600 °C under 30 sccm 5% H$_2$/N$_2$ for 2 h is 5725.5 eV, which remains the same with that from the pre-treated SCY, but an increase in the temperature to 850°C results in a slight shift towards a lower edge energy (5725.2eV), which is closer to 5719.6eV so that an average oxidation state of Ce ion very slightly closer to +3 is implied. The result is highly consistent with XPS and TPR results for SCY samples, which also suggest the excellent stability of SCY under reducing environment up to 1000°C. The XANES spectra of Ce L$_3$-edge on SCY samples were step changed with an artan shape due to the transition to continuum states with the expulsion of a photoelectron and deconvoluted into 4 peaks including pre-edge, Ce^{3+}, and two Ce^{4+}, as shown in Figure (17). The fractions of Ce^{3+} and Ce^{4+} ions in SCY samples were calculated by corresponding peak area and Equations (18) and (19) [44].

$$[Ce^{3+}] = \frac{Area\ of\ (Ce^{3+})}{Area\ of\ (Ce^{3+})\ and\ (Ce^{4+})} \tag{18}$$

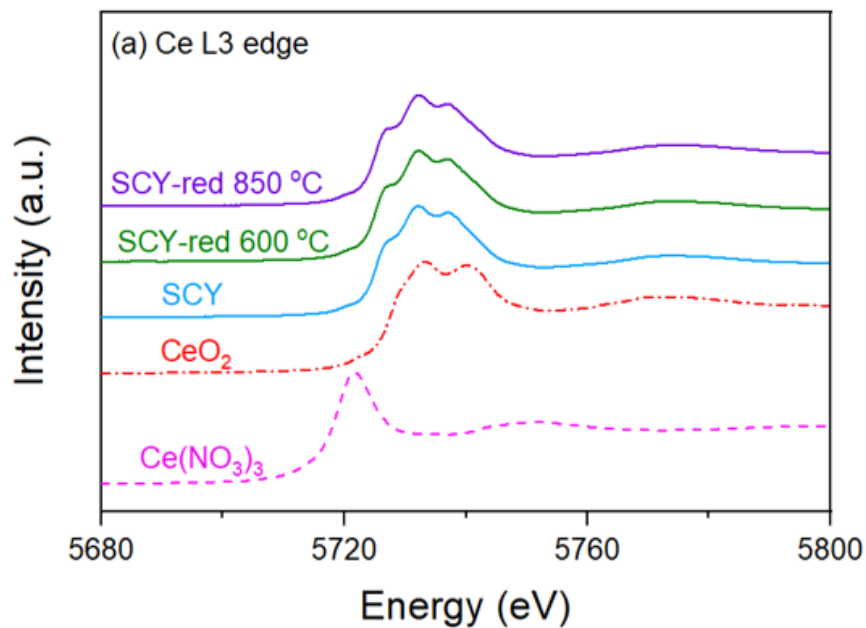$$[Ce^{4+}] = \frac{Area\ of\ (Ce^{4+})}{Area\ of\ (Ce^{3+})\ and\ (Ce^{4+})} \tag{19}$$

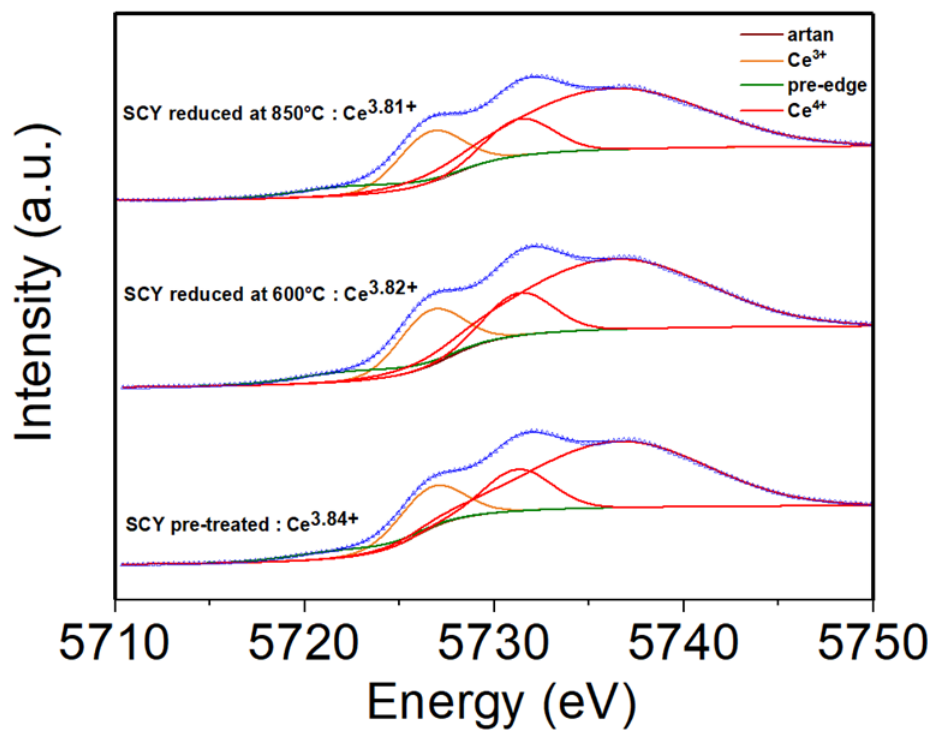Figure 16: Normalized Ce L$_3$-edge XANES spectra of SCY

Figure 17: Normalized Ce L$_3$-edge deconvolution

The average oxidation state of Ce in SCY was estimated by Athena to be 3.82 $\pm$ 0.02, indicating the mixed Ce ions with +3 and +4 oxidation states are stable under reducing environment at high temperature because of the small variation over the course of temperature elevation. The oxidation state of Mn in undoped $LaMnO_3$ is +3, but doping divalent Sr cation into the trivalent La sites creates holes and induces a mixed oxidation state of Mn ions. The XANES spectra on pre-treated LSM shows very similar edge energy of 6552.97eV to the edge energy of Mn_2O_3, which is 6552.37eV, as shown in Figure (18). The edge energy of reduced LSM at 600°C 6552.37eV is exactly the same with the edge energy of Mn_2O_3. This means the electronic structure of LSM is stable up to 600°C under reducing environment. However, a further increase in the temperature up to 850°C shifts the edge energy of Mn ions on the reduced LSM lower to 6549.67eV, which is very close to 6549.38eV on the reference Mn_3O_4 with a mixture of ions Mn^{2+} and Mn^{3+}. The oxidation state of Mn ions on pre-treated LSM is estimated to be roughly +3.1, according to the fitted relationship between oxidation state and edge energy shown in Figure 19. This demonstrates the presence of Mn^{2+} ions and the oxygen vacancies. The estimated oxidation states of Mn under reducing environment at 600°C and 850°C are +2.96 and +2.33, respectively. Since the redox performance of B-site ions is tightly related to catalytic activity, a significantly low oxidation state of Mn in LSM perovskites indicate their strong reactivity during propane ODH and their possible contribution to the over-oxidation of propane and propylene to CO_2 and CO. This result aligns with the result from XPS analysis.
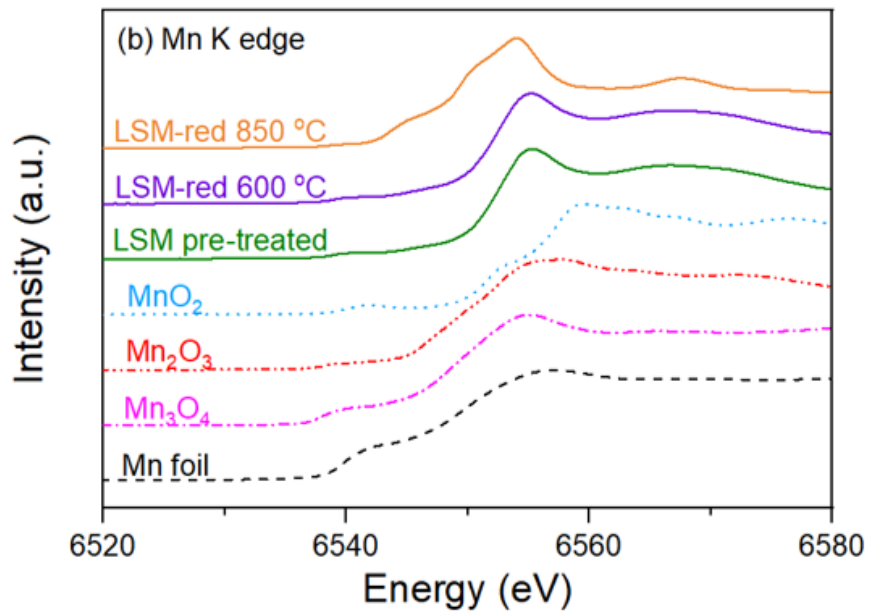
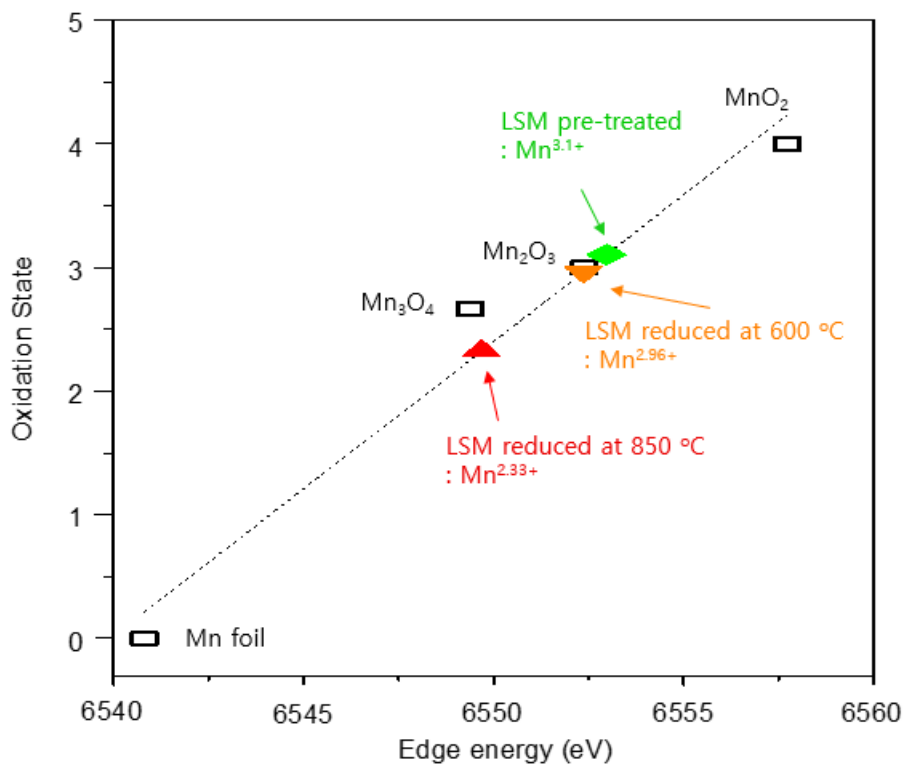**Figure 18:** Normalized Mn K-edge XANES spectra of LSM

Figure 19: Linear fit of the relationship between oxidation state of Mn and edge energy

3.4 TPrxn/TPR

TPrxn was performed to investigate the species presented in the post-reaction stream as a function of temperature. The area below the peaks corresponds to the relative quantity of products. On the SCY catalyst, propylene production starts to occur at around 600°C, accompanied by CO at 600°C and small amount of CO_2 at 700°C, as shown in Figure 20(a). At around 650°C, appreciable amount of CO produced while proplyene production is insignificant at below 700°C. On the LSM catalyst, although the production of propylene begins at a lower temperature and the quantity is higher compared to SCY, it introduces a significant amount of CO and CO_2, as shown in Figure 20(b). This testifies to the strong reactivity of LSM especially under reducing environment and its contribution to deep oxidation. A propylene TPrxn was also conducted to study the degree of over-oxidation on each catalyst. The results shown in Figure 20(c) reveal that a great amount of proplyene is oxidized to CO_2 on LSM since temperature reaches 500°C, whereas negligible amount of CO_2 production is found on the SCY catalyst. This results suggest a reduction of LSM concentration in SCY-LSM composite is desired to reduce the degree of over-oxidation.
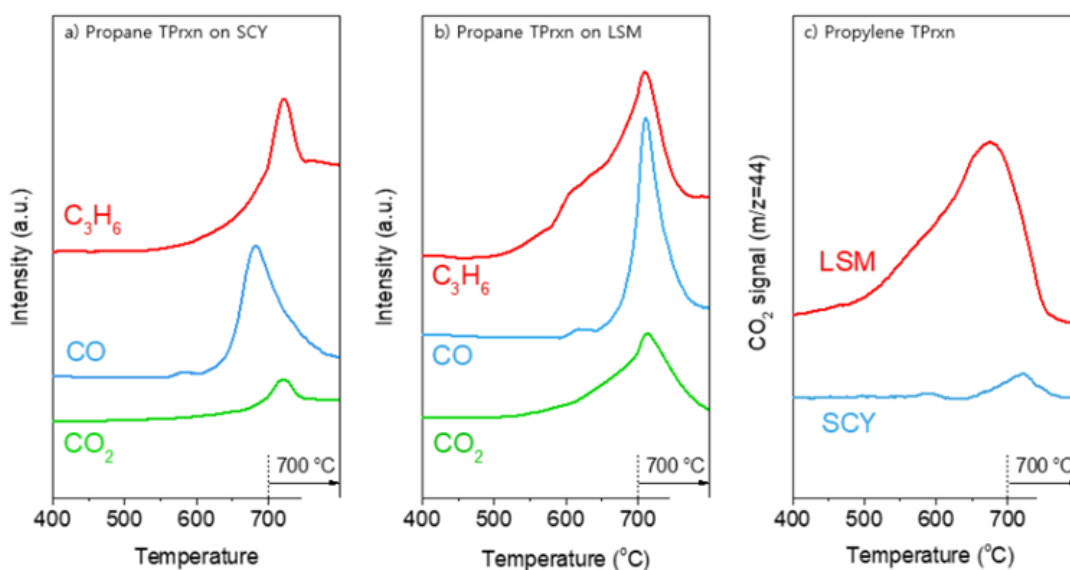

Figure 20: Temperature-programmed reaction results

TPR was performed using H_2 to study the reducibility of SCY and LSM. The catalyst samples were exposed to a flow of 30 sccm 5% H_2/N_2 while the temperature was increased gradually from room temperature to 1000°C. The area below the peaks corresponds to the quantity of H_2O as a consequence of H_2 reduction. By measuring the H_2 content at the reactor outlet, we were able to determine the total amount of hydrogen consumed. From there, the degree of reduction and average oxidation state of solid after reduction could be calculated [45]. Figure (21) shows the H_2O signal for both samples over temperature up to 1000°C. The TPR profile for SCY presents no noticeable peak, meaning no H_2O has been forming in the process. This reflects the excellent stability of SCY under reducing environment at temperature as high as 1000°C. The TPR profile for LSM shows a small peak at around 100-200°C, which is associated with the surface reduction of Mn^{4+} into Mn^{3+}. The most significant part of hydrogen consumption occurs in the temperature range of 450-600°C. In this range, the reduction reaction is dominated by the interaction of hydrogen with bulk oxygen species and simultaneous reduction of Mn^{4+} into Mn^{3+} [46]. The result of TPR provides further evidence for the strong reducibility of LSM relative to SCY which is suggested by XPS analysis.
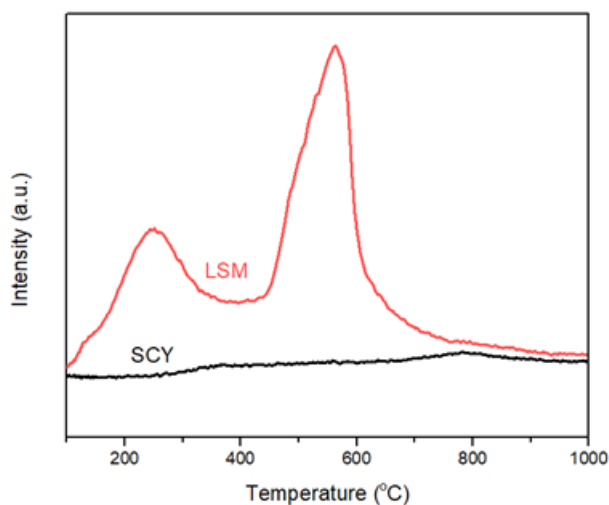

Figure 21: Temperature-programmed reduction results

31

3.5 DRIFTS

In-situ DRIFTS spectra were obtained from the temperature-programmed desorption (TPD) of CO_2 and H_2O over the temperature range of 50-450°C. The CO_2 desorption analysis facilitates the study of the surface basicity of LSM and SCY by using the acidic molecule CO_2 for probing the basic sites on the metal oxides. The main basic sites on the metal oxides are Lewis basic sites, existing primarily in the form of basic surface lattice oxygen or hydroxyl groups, which are formed due to the interaction between protons and lattice oxygen. The adsoprtion and reaction between CO_2 and hydroxyl groups may contribute to the formation of bicarbonates, while the interaction of CO_2 with basic surface lattice oxygen can result in various carbonate species, with IR features in the range 1800-800 cm^{-1} [47]. These predictions have been confirmed by DRIFTS spectra. As shown in Figure (22), the adsorption of CO_2 causes various surface species to form on SCY surface, including bicarbonates (1610 and 1212 cm^{-1}) resulted from the reactive adsorption with basic OH groups, carbonates, bidentates (1025-1060, 1295 and 1575 cm^{-1}), monodentates (1025-1060 and 1575 cm^{-1}), and bridged carbonates (1025-1060, 1295, and 1672 cm^{-1}) resulted from reactive adorption with basic surface lattice oxygen [47]. The existence of bicarbonate and carbonate vibrations on the SCY surface prove the presence of both hydroxyl groups and the lattice oxygen sites. Even at high temperatures such as 450°C, such IR bands still remain visible, which is indicative of the strong interaction between the surface active sites and the carbonate species. The Mars-van Krevelen (MvK) kinetic model for reduction - oxidation reactions of solid catalysts suggests the activation of C-H bond in hydrocarbon molecules primarily occurs on the basic lattice oxygen sites [48]. According to this, the existence of hydroxyl groups and lattice oxygen on SCY surface proved by the CO_2 TPD-DRIFTS experiment implies the promise of SCY as the anode catalyst for propane ODH. In comparison, as shown in Figure (22), DRIFTS spectra of LSM show that there is no noticeable peak under temperatures ranging from 50 to 450 °C. This indicates interaction

between CO_2 and the LSM surface sites is lacking due to the absence of carbonate species observed. This is probably attributable to the extremely weak basicity of the LSM surface, implying LSM alone may not have sufficient catalytic activity for propane ODH.
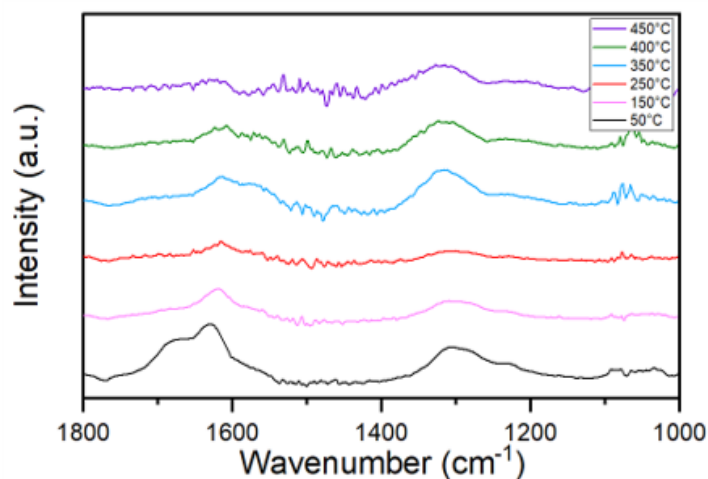

Figure 22: *In-situ* DRIFTS of CO_2 and propane on SCY from 50 to 450 °C

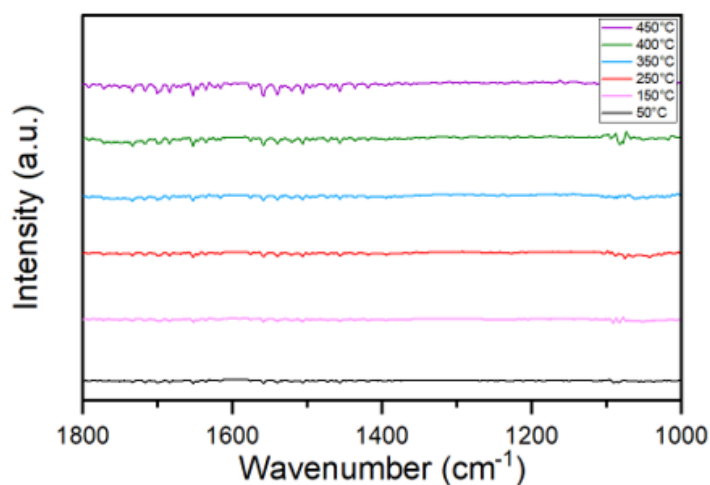**Figure 23:** *In-situ* DRIFTS of CO_2 and propane on LSM from 50 to 450 °C

In-situ DRIFTS spectra of water were obtained from the temperature-programmed desorption of water over the temperature range of 50-450°C. This analysis aims to examine the proton-conducting ability of the catalyst samples. As shown in Figure (24), a distinctive double peak (1800-1900 cm^{-1}) exists for the SCY DRIFTS profile especially under

33

lower temperatures, corresponding to the desorbed water. The evidence of the existence of adsorbed water on SCY surface reveals the strong interaction between protons and lattice oxygen as well as the efficient transport of protons between lattice oxygen, thereby suggesting the remarkable proton-conductivity of SCY under a wide range of temperatures. In comparison, Figure (25) shows no visible peak on the LSM DRIFTS profile, meaning almost no water molecule is being desorbed over the TPD process. This reflects the lack of proton-conducting mechanism in LSM.
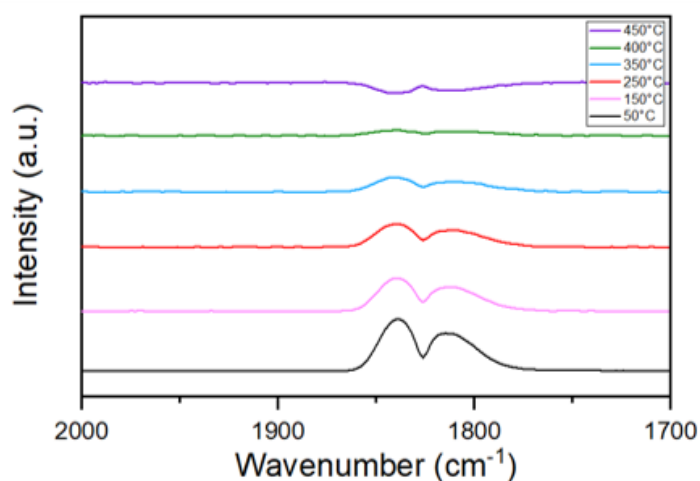

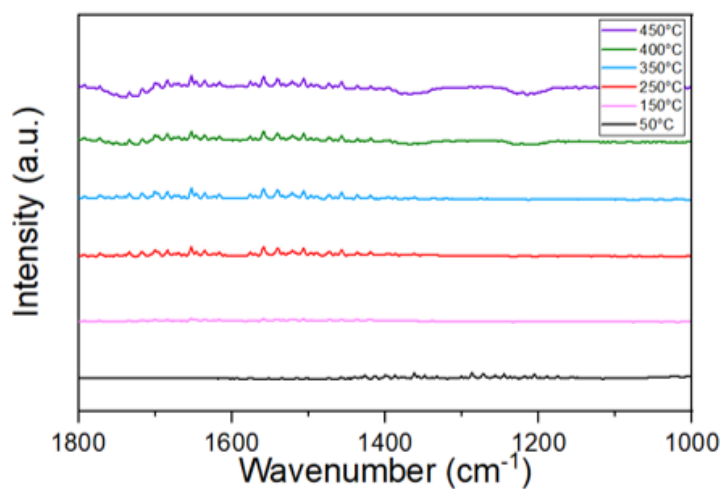**Figure 24:** *In-situ* DRIFT of H_2O and propane on SCY from 50 to 450 ℃

Figure 25: *In-situ* DRIFT of H_2O and propane on LSM from 50 to 450 ℃

Figure (26) shows the water signal as a function of temperature in range 100-600°C for SCY and LSM with He treatment and humidified He treatment with 0.1MPa H_2O, respectively. For the dry He treated sample, the SCY profile exhibits two distinctive peaks. The weaker peak at around 200°C suggests the water interaction at the catalyst surface, while the second and stronger peak at round 450C reflects the existence of bulk water inside SCY. In comparison, the LSM profile only shows a small peak at 200°C, suggesting extremely weak water adsorption. When SCY is treated with humidified He with 0.1MPa water, only the stronger peak exists at 450°C, meaning the water interaction at the catalyst surface is lacking, but there is still bulk water present in the SCY lattice. The LSM profile shows no peak, which is consistent with the result from He treatment.
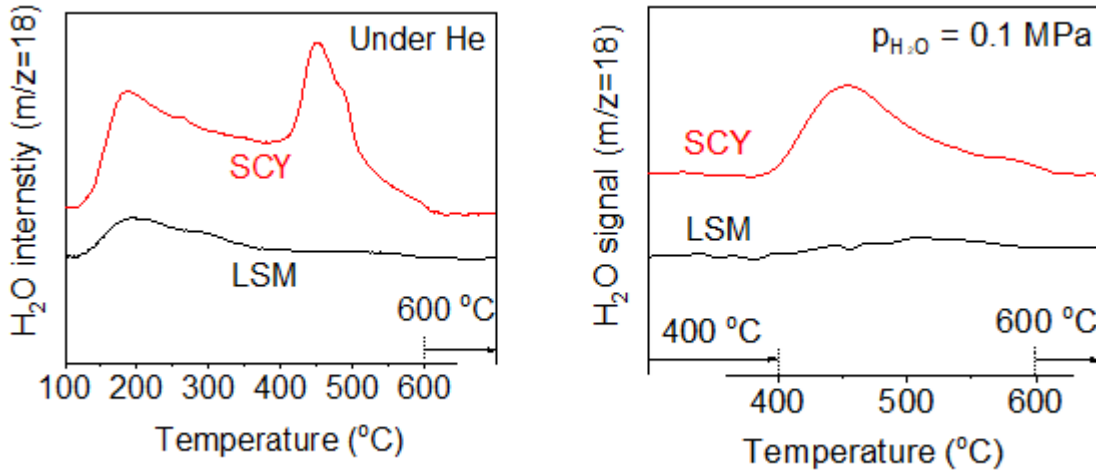
Figure 26: H_2O signal for SCY and LSM from 400 to 600°C

3.6   Electrochemical activity measurements

Electrical conductivity was measured by 4-probe DC van der Pauw method from 25 to 600°C for SCY-LSM composites. The results are plotted in Figure (27). As hypothesized, the pure as-synthesized SCY without the addition of LSM exhibits limited conductivity. Its electrical conductivity is almost negligible below 200°C, but rises to 4.5 $\times 10^{-4} \sigma$ cm^{-1} at

600°C, although still not appreciable for propane ODH. Mixing SCY with LSM significantly enhances the electrical conductivity. The SCY and LSM mixture with SCY:LSM 8:2 ratio demonstrates much higher conductivity than the as-synthesized SCY, reaching 0.05S/cm at 600°C. This is because of the presence of LSM, which has an electrical conductivity of 153S/cm cm^{-1} at 600°C at its pure phase. The mixture of SCY and LSM exhibits intermediate electrical conductivity between that of their pure phases. An increase in the composition of LSM in SCY-LSM significantly boosts the electrical conductivity at any temperature. The biggest improvement in terms of electrical conductivity of the mixture occurs when increasing the SCY concentration from 20% to 40%, suggesting SCY:LSM 6:4 is likely the optimal composition that has both reasonable electrical conductivity and protonic conductivity. The activation energy for hopping polarons increases significantly in proportion to the increase in SCY composition, as summarized in Table (3) and demonstrated by the slopes of the fitted linear curves in Figure (28). This is likely because LSM features the presence of polaron conduction in its lattice, as introduced previously, but SCY has no such conduction mechanism in its lattice. Interesting, SCY:LSM 2:8 exhibits the lowest activation energy as 0.11eV, even lower than that of pure LSM. The reason behind this abnormality is unknown.

Sample	Slope	Activation energy (eV)
SCY:LSM 8:2	-2.89	0.25
SCY:LSM 6:4	-2.37	0.2
SCY:LSM 4:6	-1.72	0.15
SCY:LSM 2:8	-1.22	0.11
LSM	-1.44	0.12

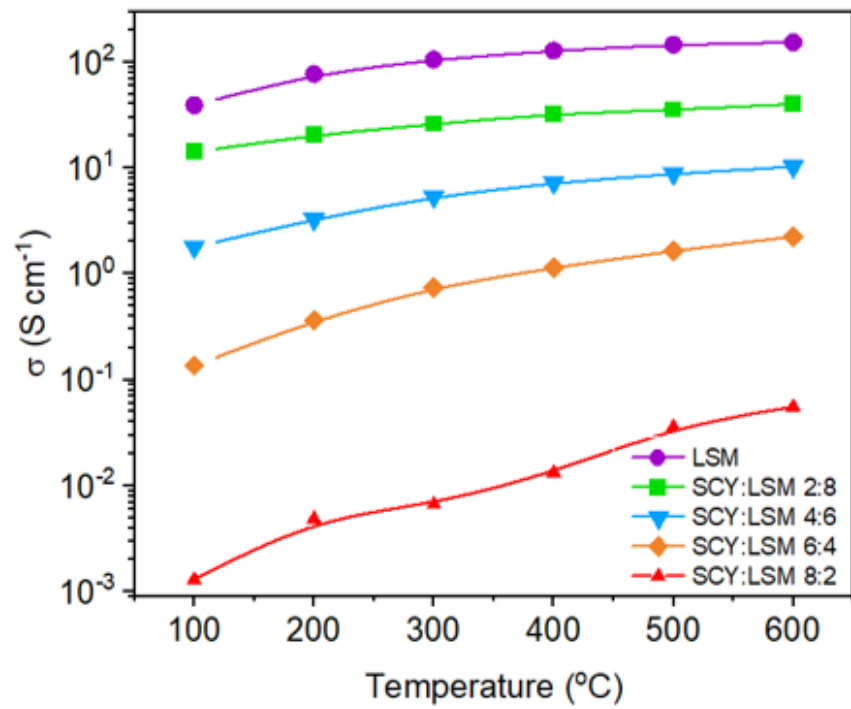**Table 3:** A summary of activation energy of catalyst mixtures

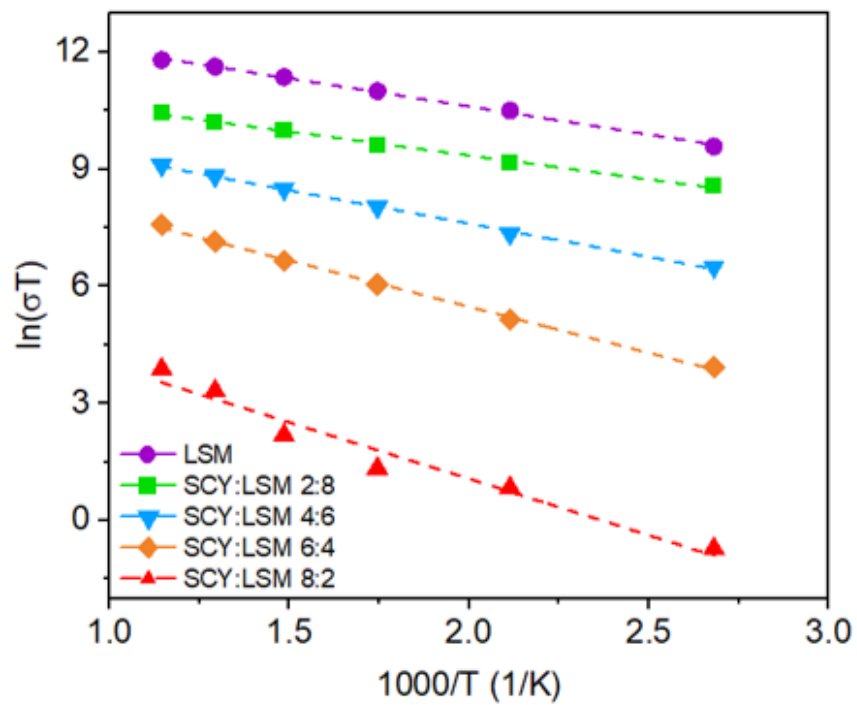**Figure 27:** Electrical conductivity of SCY-LSM mixed catalyst

Figure 28: Activation energy of SCY-LSM mixed catalyst

3.7 Electrocatalytic propane ODH

Figure (29) summarizes the performance of propane ODH in a SOEC with SCY-LSM as the anode at different mixing ratio. The propane ODH process produces carbon-containing compounds such as C_3H_6, C_2H_4, CH_4, CO, and CO_2. By using a current of 5mA, the selectivity of propylene remains constant at around 24% for any composition. The selectivity of alkenes is enhanced slightly from roughly 52% to 57% by mixing SCY with LSM, but increasing the SCY composition has no further effect on alkenee selectivity. This reflects that the composition of SCY may only have a limited effect on propylene selectivity among all products. However, with the increase in the composition of SCY from 0% to 80%, the production of CO and CO_2 was significantly reduced. In other words, the alkene/CO_x selectivity increases significantly from 2.3 for pure LSM catalyst to 6.5 for SL82. This is in good agreement with the reactive property of LSM, whose presence is responsible for the deep oxidation of propylene and subsequently favors the production of CO and CO_2. From these results, it is evident that mixing SCY could mitigate the degree of over-oxidation, while ensuring the propylene selectivity is not undermined. Figure (29) also suggests the trend of propane conversion with respect to the mixing ratio of SCY-LSM. The highest propane conversion is achieved by pure LSM ($\sim$75%), but drops significantly ($\sim$35%) once the SCY phase is introduced. A further increase in SCY composition has a very minor impact on the propane conversion. This is likely an indicative of electron transfer limitation because mixing poorly electrical conductive SCY is detrimental to the electrical conductivity of the composite, resulting in a lack of energy efficiency.
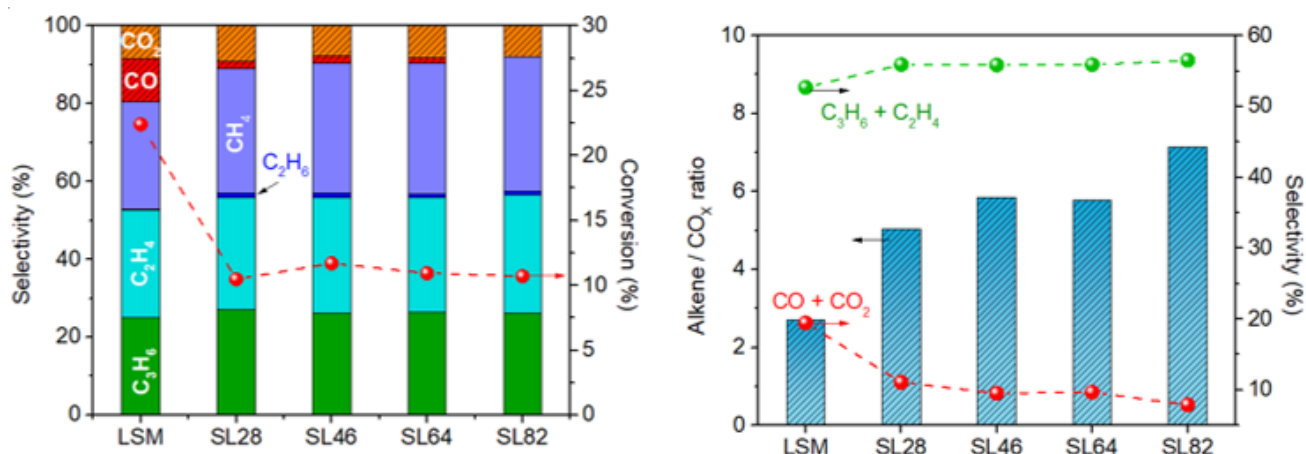
Figure 29: Propane conversion and product selectivity of SCY-LSM mixed catalyst

Figure (30) shows the enhancement ratio of propylene and ethylene yields from Open Circuit Voltage (OCV) for SCY:LSM 4:6 at 600°C. The conversion of propane increases from 5% under OCV to 20% under 20mA. The use of 20 mA boosts propylene selectivity and ethylene selectivity by 125% and 170%, respectively. This indicates the strong and position effect of applied current on both the conversion of propane and the selectivity of alkenes. Hence, using a high applied current is an effective but energy-consuming approach to overcome the lowered propane conversion issue during propane ODH due to SCY mixing.
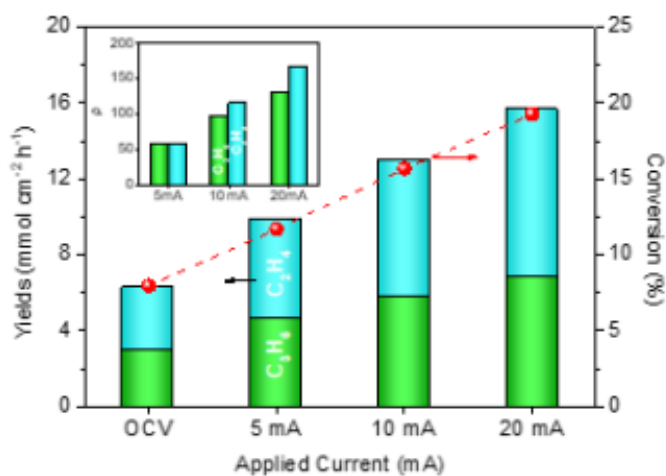

Figure 30: Enhancement ratio of propylene and ethylene yields from OCV

39

4 Conclusions

In this study, we developed an electrocatalytically-assisted oxidative propane dehydrogenation process for propylene production using a solid oxide electrolysis cell. Dual phase proton-conducting ytterbium-doped strontium cerate mixed with electron and oxide ion-conducting strontium-doped lanthanum manganite was investigated as a promising anode catalyst. It was observed that mixing SCY with LSM enhanced the electrical conductivity by orders of magnitude. Although the incorporation of SCY had no visible effect on propylene selectivity and a minor but positive impact on alkene selectivity, it was discovered the increased composition in SCY could facilitate the suppression of CO_x selectivity. Introducing small quantity of SCY into LSM significantly lowered the propane conversion, but no significant further impact on the propane conversion was observed with high fractions of SCY. It might be also suggested that the low selectivity issue could be partially solved by using higher applied current. However, the development of this technology is on-going and substantial efforts are needed to devote into the further investigations in order to achieve commercially feasible propane conversion and propylene selectivity.

References

[1] Aaron Akah and Musaed Al-Ghrami. Maximizing propylene production via fcc technology. *Applied Petrochemical Research*, 5(4):377–392, 2015.

[2] MM Bhasin, JH McCain, BV Vora, T Imai, and PR Pujado. Dehydrogenation and oxydehydrogenation of paraffins to olefins. *Applied Catalysis A: General*, 221(1-2):397–419, 2001.

[3] Seval Gunduz, Doruk Dogu, Dhruba J Deka, Katja E Meyer, Anshuman Fuller, Anne C Co, and Umit S Ozkan. Application of solid electrolyte cells in ion pump and electrolyzer modes to promote catalytic reactions: An overview. *Catalysis Today*, 323:3–13, 2019.

[4] Huiyuan Zhu, Pengfei Zhang, and Sheng Dai. Recent advances of lanthanum-based perovskite oxides for catalysis. *ACS Catalysis*, 5(11):6370–6385, 2015.

[5] Wang Hay Kan, Alfred Junio Samson, and Venkataraman Thangadurai. Trends in electrode development for next generation solid oxide fuel cells. *Journal of Materials Chemistry A*, 4(46):17913–17932, 2016.

[6] Tatsumi Ishihara. *Perovskite oxide for solid oxide fuel cells.* Springer Science & Business Media, 2009.

[7] Emiliana Fabbri, Daniele Pergolesi, and Enrico Traversa. Materials challenges toward proton-conducting oxide fuel cells: a critical review. *Chemical Society Reviews*, 39(11):4355–4369, 2010.

[8] Doruk Dogu, Katja E Meyer, Anshuman Fuller, Seval Gunduz, Dhruba J Deka, Nathaniel Kramer, Anne C Co, and Umit S Ozkan. Effect of lanthanum and chlorine doping on strontium titanates for the electrocatalytically-assisted oxidative dehydrogenation of ethane. *Applied Catalysis B: Environmental*, 227:90–101, 2018.

[9] SHN Lim, DR McKenzie, and MMM Bilek. Van der pauw method for measuring resistivity of a plane sample with distant boundaries. *Review of scientific instruments*, 80(7):075109, 2009.

[10] Jesper JHB Sattler, Javier Ruiz-Martinez, Eduardo Santillan-Jimenez, and Bert M Weckhuysen. Catalytic dehydrogenation of light alkanes on metals and metal oxides. *Chemical reviews*, 114(20):10613–10653, 2014.

[11] Eric M Karp, Todd R Eaton, Violeta Sànchez i Nogué, Vassili Vorotnikov, Mary J Biddy, Eric CD Tan, David G Brandner, Robin M Cywar, Rongming Liu, Lorenz P Manker, et al. Renewable acrylonitrile production. *Science*, 358(6368):1307–1310, 2017.

[12] Richard F Fansler, Paul Taheri, Carey Cullinane, Braulio Sabates, and Lewis M Flint. Polypropylene mesh closure of the complicated abdominal wound. *The American journal of surgery*, 170(1):15–18, 1995.

[13] Ismaël Amghizar, Laurien A Vandewalle, Kevin M Van Geem, and Guy B Marin. New trends in olefin production. *Engineering*, 3(2):171–178, 2017.

[14] F Cavani and F Trifiro. The oxidative dehydrogenation of ethane and propane as an alternative way for the production of light olefins. *Catalysis Today*, 24(3):307–313, 1995.

[15] Farnaz Tahriri Zangeneh, Abbas Taeb, Khodayar Gholivand, and Saeed Sahebdelfar. Thermodynamic equilibrium analysis of propane dehydrogenation with carbon dioxide and side reactions. *Chemical Engineering Communications*, 203(4):557–565, 2016.

[16] Tao Ren, Martin Patel, and Kornelis Blok. Olefins from conventional and heavy feedstocks: Energy use in steam cracking and alternative processes. *Energy*, 31(4):425–451, 2006.

[17] Dhruba J Deka, Jaesung Kim, Seval Gunduz, Deeksha Jain, Yingjie Shi, Jeffrey T Miller, Anne C Co, and Umit S Ozkan. Coke formation during high-temperature co2 electrolysis over afeo3 (a= la/sr) cathode: Effect of a-site metal segregation. *Applied Catalysis B: Environmental*, 283:119642, 2021.

[18] Mohd Bismillah Ansari and Sang-Eon Park. Carbon dioxide utilization as a soft oxidant and promoter in catalysis. *Energy & Environmental Science*, 5(11):9419–9437, 2012.

[19] Matthew P Woods, Burcu Mirkelamoglu, and Umit S Ozkan. Oxygen and nitrous oxide as oxidants: Implications for ethane oxidative dehydrogenation over silica- titania-supported molybdenum. *The Journal of Physical Chemistry C*, 113(23):10112–10119, 2009.

[20] Tushar Choudhary et al. Thermodynamic assessment of sofc-icgt hybrid cycle: Energy analysis and entropy generation minimization. *Energy*, 134:1013–1028, 2017.

[21] Kaidong Chen, Alexis T Bell, and Enrique Iglesia. Kinetics and mechanism of oxidative dehydrogenation of propane on vanadium, molybdenum, and tungsten oxides. *The Journal of Physical Chemistry B*, 104(6):1292–1299, 2000.

[22] S Heiroth, Thomas Lippert, Alexander Wokaun, M Döbeli, JLM Rupp, B Scherrer, and Ludwig J Gauckler. Yttria-stabilized zirconia thin films by pulsed laser deposition: Microstructural and compositional control. *Journal of the European Ceramic Society*, 30(2):489–495, 2010.

[23] Fanglin Chen and Meilin Liu. Preparation of yttria-stabilized zirconia (ysz) films on la0. 85sr0. 15mno3 (lsm) and lsm–ysz substrates using an electrophoretic deposition (epd) process. *Journal of the European Ceramic Society*, 21(2):127–134, 2001.

[24] Kai Sundmacher, LK Rihko-Struckmann, and Vladimir Galvita. Solid electrolyte membrane reactors: Status and trends. *Catalysis Today*, 104(2-4):185–199, 2005.

[25] Hyunmin Kim, Sangwook Joo, Ohhun Kwon, Sihyuk Choi, and Guntae Kim. Cobalt-free pr0. 5ba0. 4sr0. 1feo3-δ as a highly efficient cathode for commercial ysz-supported solid oxide fuel cell. *ChemElectroChem*, 7(21):4378–4382, 2020.

[26] RO Fuentes and RT Baker. Synthesis and properties of gadolinium-doped ceria solid solutions for it-sofc electrolytes. *International Journal of Hydrogen Energy*, 33(13):3480–3484, 2008.

[27] Jeffrey W Fergus. Oxide anode materials for solid oxide fuel cells. *Solid State Ionics*, 177(17-18):1529–1541, 2006.

[28] AJ Jacobson, C Yu, and W Gong. Thin-film solid oxide fuel cell (sofc) materials. In *Functional Materials for Sustainable Energy Applications*, pages 478–514. Elsevier, 2012.

[29] AK Demin, PE Tsiakaras, VA Sobyanin, and S Yu Hramova. Thermodynamic analysis of a methane fed sofc system based on a protonic conductor. *Solid State Ionics*, 152:555–560, 2002.

[30] Tongtong Wang, Hongyu Zhang, Bo Meng, Xiaobin Wang, Jaka Sunarso, Xiaoyao Tan, and Shaomin Liu. Srce 0.95 y 0.05 o 3- δ–zno dual-phase membranes for hydrogen permeation. *RSC Advances*, 6(43):36786–36793, 2016.

[31] Kevin S Knight and Nicholas Bonanos. The crystal structures of some doped and undoped alkaline earth cerate perovskites. *Materials Research Bulletin*, 30(3):347–356, 1995.

[32] N Bonanos, B Ellis, and MN Mahmood. Oxide ion conduction in ytterbium-doped strontium cerate. *Solid State Ionics*, 28:579–584, 1988.

[33] Guanghua Yi, Takashi Hayakawa, Arnfinn G Andersen, Kunio Suzuki, Satoshi Hamakawa, Andrew PE York, Masao Shimizu, and Katsuomi Takehira. Oxidative

dehydrogenation of ethane over la 1- x sr x feo 3- δ perovskite oxides. *Catalysis letters*, 38(3):189–195, 1996.

[34] Jens Ranløv and Kurt Nielsen. Crystal structure of the high-temperature protonic conductor srceo 3. *Journal of Materials Chemistry*, 4(6):867–868, 1994.

[35] TJB Holland and SAT Redfern. Unit cell refinement from powder diffraction data; the use of regression diagnostics. *Mineralogical Magazine*, 61(1):65–77, 1997.

[36] S Ponce, MA Peña, and JLG Fierro. Surface properties and catalytic performance in methane combustion of sr-substituted lanthanum manganites. *Applied Catalysis B: Environmental*, 24(3-4):193–205, 2000.

[37] Dhruba J Deka, Seval Gunduz, Taylor Fitzgerald, Jeffrey T Miller, Anne C Co, and Umit S Ozkan. Production of syngas with controllable h2/co ratio by high temperature co-electrolysis of co2 and h2o over ni and co-doped lanthanum strontium ferrite perovskite cathodes. *Applied Catalysis B: Environmental*, 248:487–503, 2019.

[38] M Bevilacqua, Tiziano Montini, Claudio Tavagnacco, Gianpaolo Vicario, Paolo Fornasiero, and Mauro Graziani. Influence of synthesis route on morphology and electrical properties of lani0. 6fe0. 4o3. *Solid State Ionics*, 177(33-34):2957–2965, 2006.

[39] D Grossin and JG Noudem. Synthesis of fine la0. 8sr0. 2mno3 powder by different ways. *Solid State Sciences*, 6(9):939–944, 2004.

[40] Kevin S Knight. Structural and thermoelastic study of the protonic conducting perovskite srce 0.95 yb 0.05 o ξ (ξ 3) between 373 k and 1273 k. *Journal of electroceramics*, 27(3):143–153, 2011.

[41] Shaomin Liu, K Li, and R Hughes. Preparation of srce0. 95yb0. 05o3- α perovskite for use as a membrane material in hollow fibre fabrication. *Materials research bulletin*, 39(1):119–133, 2004.

[42] Jim Matthew. Surface analysis by auger and x-ray photoelectron spectroscopy. d. briggs and jt grant (eds). impublications, chichester, uk and surfacespectra, manchester, uk, 2003. 900 pp., isbn 1-901019-04-7, 900 pp, 2004.

[43] AV Soldatov, TS Ivanchenko, S Della Longa, A Kotani, Y Iwamoto, and A Bianconi. Crystal-structure effects in the ce l 3-edge x-ray-absorption spectrum of ceo 2: Multiple-scattering resonances and many-body final states. *Physical Review B*, 50(8):5074, 1994.

[44] Tai-Sing Wu, Yunyun Zhou, Renat F Sabirianov, Wai-Ning Mei, Yun-Liang Soo, and Chin Li Cheung. X-ray absorption study of ceria nanorods promoting the disproportionation of hydrogen peroxide. *Chemical Communications*, 52(28):5003–5006, 2016.

[45] MA Reiche, M Maciejewski, and A Baiker. Characterization by temperature programmed reduction. *Catalysis today*, 56(4):347–355, 2000.

[46] Virginie Roche, A Hadjar, JP Deloume, Thierry Pagnier, R Revel, Claude Roux, Elisabeth Siebert, and Philippe Vernoux. Physicochemical origins of electrochemical promotion of lsm/ysz. *Catalysis Today*, 146(3-4):266–273, 2009.

[47] Zili Wu, Amanda KP Mann, Meijun Li, and Steven H Overbury. Spectroscopic investigation of surface-dependent acid–base property of ceria nanoshapes. *The Journal of Physical Chemistry C*, 119(13):7340–7350, 2015.

[48] M Markova-Velichkova, T Lazarova, V Tumbalev, G Ivanov, D Kovacheva, P Stefanov, and A Naydenov. Complete oxidation of hydrocarbons on yfeo3 and lafeo3 catalysts. *Chemical engineering journal*, 231:236–244, 2013.